Whole-Voltage-Range Solid-Solution Reaction in Layered Oxide Cathode of Sodium-Ion Batteries

*Meng Ren, Zhuo Zhu, Zhaohui Liang, Yaohui Huang, Tong Zhang, Machuan Hou, Kai Zhang, Zonghai Chen, Yushi He, Zifeng Ma, Jun Chen and Fujun Li**

M. Ren, Z. Zhu, Z. Liang, Y. Huang, T. Zhang, M. Hou, Prof. K. Zhang, Prof. J. Chen, Prof. F. Li
Key Laboratory of Advanced Energy Materials Chemistry (Ministry of Education), Renewable Energy Conversion and Storage Center (RECAST), College of Chemistry, Nankai University
Tianjin 300071 (China)
E-mail: fujunli@nankai.edu.cn

Prof. K. Zhang, Prof. J. Chen, Prof. F. Li
Haihe Laboratory of Sustainable Chemical Transformations
Tianjin 300071 (China)

Prof. Z. Chen
Chemical Sciences and Engineering Division, Argonne National Laboratory, 9700 South Cass Avenue
Lemont IL 60439 (USA)

Prof. Y. He, Prof. Z. Ma
Shaoxing Institute of New Energy and Molecular Engineering, Shanghai Jiao Tong University
Shaoxing 312300 (China)

Keywords: solid-solution reaction, layered oxides, electron population, cycle stability, sodium-ion batteries

Layered manganese-based oxides are promising cathode materials for sodium-ion batteries due to their versatile structures. However, the Jahn–Teller effect of Mn^{3+} induces severe distortion of MnO_6 octahedra, and the resultant low symmetry is responsible for gliding of MnO_2 layers and then inferior multiple phase transitions upon Na^+ extraction/insertion. Here, hexagonal P2-

$Na_{0.643}Li_{0.078}Mn_{0.827}Ti_{0.095}O_2$ is synthesized through the incorporation of Li and Ti into the distorted orthorhombic P'2-$Na_{0.67}MnO_2$ to function as a phase-transition-free oxide cathode. It is revealed that Li in both the transition-metal and Na layers enhances the covalency of Mn-O bonds and allows degeneracy of Mn *3d* e_g orbitals to favor formation of hexagonal phase; and high strength of Ti-O bonds reduces the electrostatic interaction between Na and O for suppressed Na^+/vacancy rearrangements. These collectively lead to a whole-voltage-range solid-solution reaction between 1.8 and 4.3 V with small volume variation of 1.49%. This rewards its excellent cycling stability (capacity retention of 90.2% after 500 cycles) and rate capability (95.5 mAh g^{-1} at 2000 mA g^{-1}).

1. Introduction

Layered manganese-based oxides (LMOs) are intensively studied as cathode materials for sodium-ion batteries (SIBs) because of the rich Mn-resources, tunable structures, and facile synthesis.[1] Their structural configurations and electrochemical behaviors are intimately associated with the electron population of Mn *3d* orbitals.[2] The single-electron filled e_g ($d_{x^2-y^2}$, d_{z^2}) orbitals of high-spin Mn^{3+} (t_{2g}^3-e_g^1) induce energy level splitting of the orbitals and severe Jahn-Teller distortion of MnO_6 octahedra. It is accompanied by the geometrical distortion of LMOs to lower their symmetry and suppress the orbital degeneracy. The low-symmetry structures are susceptible to gliding of MnO_2 slabs, thus leading to inferior phase transitions and electrochemical performance deterioration upon repeated Na^+ extraction/insertion.[3] This necessitates modulation of the electron population in the Mn *3d* orbitals for improved structure stability and electrochemical performance.

P2-$Na_{0.67}MnO_2$ has been widely applied as a host material with a hexagonal symmetry for its two-dimensional Na^+ diffusion channels. It consists of two MnO_2 slabs and sandwiched Na layers in each unit cell with ABBA oxygen stacking sequences.[4] It can also crystallize into a distorted polymorph of P'2-$Na_{0.67}MnO_2$ with an orthorhombic symmetry upon quenching, which exhibits a higher capacity of up to 216 mAh g^{-1}.[5] Nevertheless, both of the two polymorphs suffer from inferior multiple phase transitions and Na^+/vacancy rearrangement, induced by the Jahn-Teller active Mn^{3+} during cycles.[6] This consequently results in their quick performance degradation.

Cation substitution with Mg^{2+}, Ni^{2+}, Ti^{4+} or Cu^{2+} in transition-metal oxide (TMO_2) layers has been widely used to improve the electrochemical performance of P'2-$Na_{0.67}MnO_2$.[6-7] The incorporation of Ti can effectively suppress the Na^+/vacancy rearrangements during Na^+ extraction/insertion.[8] However, the phase transition of P'2↔OP4 at high voltages is rarely

prevented, which results in deteriorated structure and cycle instability.[9] Li^+ doping was attempted to suppress the phase transition of P2↔O2 in P2-$Na_{0.80}[Li_{0.12}Ni_{0.22}Mn_{0.66}]O_2$ below 4.4 V, thereby improving its Na^+ storage stability.[10] Similar effects were also observed in Li-substituted O3-type materials.[11] It was reported that Li^+ doped in the TMO_2 layers improves the reversible phase transition of O3↔P3 and enables long cycle life of O3-$Na_{0.85}Li_{0.1}Ni_{0.175}Mn_{0.525}Fe_{0.2}O_2$.[11b] These suggest that either Ti- or Li-doping does improve the reversibility of phase transitions, but cannot mitigate them in P2- and O3-type oxide cathodes.

Herein, a phase-transition-free oxide cathode material is synthesized with co-doping of Li and Ti for hexagonal P2-$Na_{0.643}Li_{0.078}Mn_{0.827}Ti_{0.095}O_2$. The dopant of Li reinforces the covalency of the Mn-O bonds to eliminate the Jahn-Teller effect for symmetric MnO_6 octahedra. The Ti-O bonds reduces the electrostatic attraction between Na and O to enlarge the Na layer spacing and suppress Na^+/vacancy rearrangements. *In-situ* X-ray diffraction (XRD) indicates its phase-transition-free process with small volume variation of 1.49%, which favors the fast Na^+ diffusion in the Na layers with low migration barrier of 0.206 eV. These lead to capacity retention of 90.2% after 500 cycles at 250 mA g^{-1} and 95.5 mAh g^{-1} at 2000 mA g^{-1}.

2. RESULTS

2.1. Characterization and Analysis

The layered oxides $Na_{0.67}Li_xMn_{0.90-x}Ti_{0.10}O_2$ with different amounts of Li substitution (x = 0, 0.05, 0.08 and 0.10) and P'2-$Na_{0.67}MnO_2$ were synthesized via solid-state reactions, as described in Supporting Information. Their stoichiometry was estimated to be $Na_{0.630}Mn_{0.908}Ti_{0.092}O_2$ (NLMT-0), $Na_{0.653}Li_{0.047}Mn_{0.858}Ti_{0.095}O_2$ (NLMT-5), $Na_{0.643}Li_{0.078}Mn_{0.827}Ti_{0.095}O_2$ (NLMT-8), $Na_{0.632}Li_{0.095}Mn_{0.806}Ti_{0.099}O_2$ (NLMT-10) and $Na_{0.649}MnO_2$ (P'2-NM) by inductively coupled plasma (ICP) analyses in Table S1. Their structure characteristics were revealed by XRD in **Figure 1**a, where Ti ions disorderedly reside in the MnO_2 slabs without superstructure diffraction peaks. P'2-NM and NLMT-0 adopt a typical orthorhombic P'2 structure with a space group of *Cmcm*.[5a] Both hexagonal P2 structure with a space group of $P6_3/mmc$ and P'2 structure are observed in NLMT-5. With further increased Li contents, pure P2 structure is obtained in NLMT-8 and NLMT-10. This trend indicates that the distorted orthorhombic structure is suppressed with Li substitution, as illustrated in Figure 1b.

The Rietveld refined XRD patterns in Figure 1c and S1 indicate that NLMT-5 consists of 19.22 wt% P'2 and 80.78 wt% P2 phases, and their refined structure parameters are listed in Table S2-S7. The spacings of Na layers and TMO_2 slabs are determined to 3.769 and 1.885 Å in NLMT-0, respectively, as well as 3.649 and 1.972 Å in P'2-NM. It suggests that Ti doping

leads to shrinkage of TMO_2 slabs and enlargement of Na layers because of reduction of the electrostatic interaction between Na and O.[12] The Na layer spacing of Li-substituted $Na_{0.67}Li_xMn_{0.90-x}Ti_{0.10}O_2$ is enlarged from 3.726 to 3.788 Å along the c-axis as *x* increases from 0 to 0.08, while it contracts to 3.751 Å as *x* further increases to 0.10 because of the large radius of Li^+.[13] The largest Na layer spacing of 3.778 Å for NLMT-8 agrees well with its leftmost (002) diffraction peak in Figure 1a. The enlarged Na layer spacing and suppressed orthorhombic distortion in NLMT-8 may favor facile Na^+ movement and structure stability.

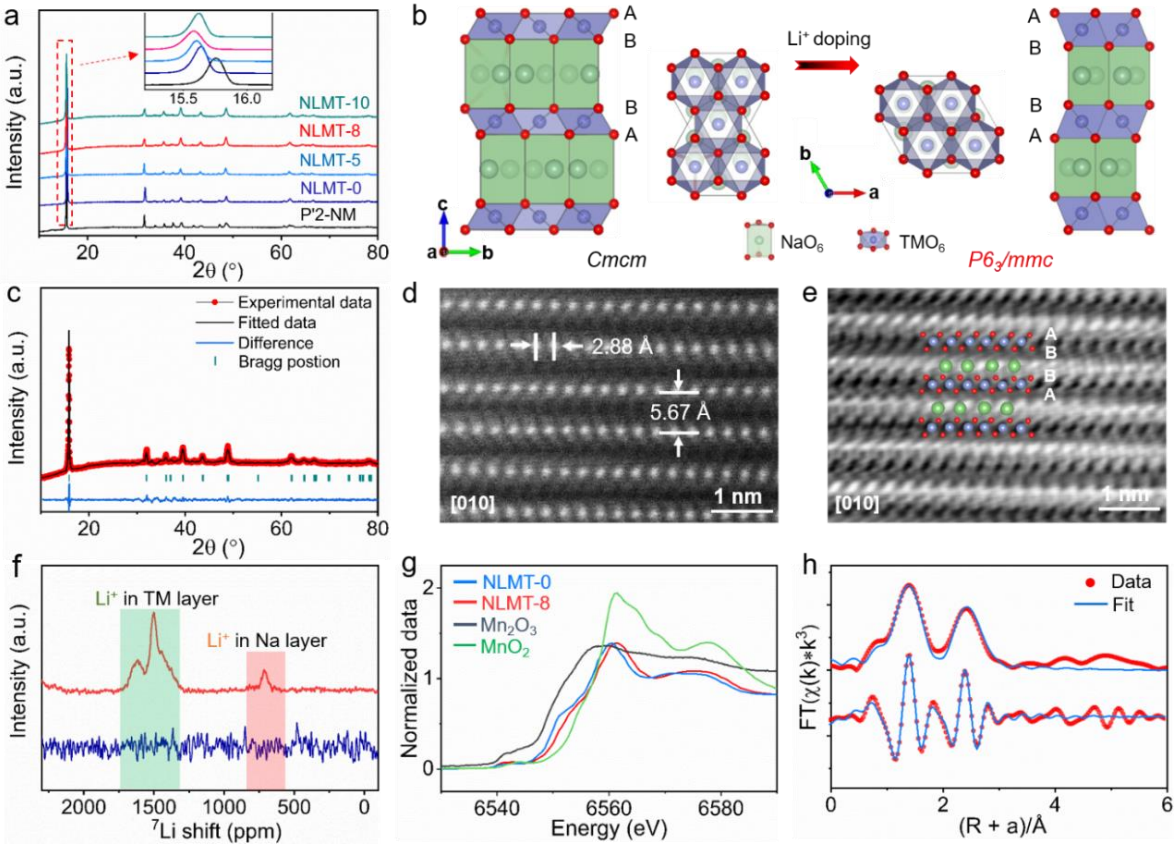

Figure 1. Structure analysis. (a) XRD patterns of P'2-NM, NLMT-0, NLMT-5, NLMT-8 and NLMT-10. (b) Crystallographic evolution of NLMT-x (x = 0, 5, 8 and10) with Li substitution. (c) XRD Rietveld refinement of NLMT-8. (d) HAADF- and (e) ABF-STEM images of NLMT-8 at the [010] zone axis. (f) ^{7}Li NMR spectra of NLMT-8. (g) XANES spectra at the Mn K-edges for NLMT-0 and NLMT-8. (h) EXAFS at the Mn K-edge and fitting results of NLMT-8 in R-space.

Atomic structures of NLMT-8 were revealed in Figure 1d and 1e by scanning transmission electron microscopy (STEM) equipped with high-angle annular dark field (HAADF) and annular bright field (ABF) techniques. The distances of the adjacent layers and TMs in HAADF-STEM image are measured to be 5.67 and 2.88 Å, respectively, which are consistent with the refined parameters in Table S5 and S7. The ABF-STEM image at the [010] zone axis reveals the arrangement of O columns with an ABBA-stacking sequence in the inset of Figure 1e. This corresponds to the typical P2 structure with hexagonal symmetry, in agreement with

the XRD patterns in Figure 1a and 1c. The scanning electron microscope (SEM) images show that NLMT-x (x = 0, 0.05, 0.08 and 0.10) have similar morphologies of plates, 3-5 μm in thickness and tens of micrometers in size, to P'2-NM in Figure S2. High-resolution transmission electron microscopy (HRTEM) images show the enlarged (002) lattice spacings of 5.65 and 5.67 Å for NLMT-0 and NLMT-8, respectively, as well as 5.62 Å for P'2-NM in Figure S3-S5. These are consistent with the refined parameters in Table S7. The energy-dispersive spectroscopy (EDS) mappings in Figure S3-S5 indicate that the elements of Na, Mn, Ti and O are uniformly distributed in P'2-NM, NLMT-0 and NLMT-8. Electron energy loss spectroscopy (EELS) measurements were carried out to show the slight differences in elemental concentration between the center and edge areas of NLMT-8 in Figure S6 and S7. In particular, the signal of Li has an extra peak around 50 eV in Figure S7, suggesting that Li^+ is located in distinct chemical environments.[14]

Solid-state ^{7}Li Nuclear Magnetic Resonance (NMR) was employed to identify the local environments of Li^+ in NLMT-8. Three resonances are observed in Figure 1f: the two at 1600 and 1450 ppm can be attributed to Li^+ sat in TMO_2 slabs, and the one at 750 ppm is assigned to Li^+ in the Na layers.[15] Their relative amount is quantified as 83% and 17%, respectively. The highly ionic nature of Li-O bonds strengthens the surrounding Mn-O bonds, as evidenced by the right-shifted Mn K-edge of the normalized X-ray absorption near-edge structure (XANES) for NLMT-8 in Figure 1g. Fourier transform extended X-ray absorption fine structures (EXAFS) are fitted to investigate the local structures of Mn in NLMT-8 and NLMT-0 in Figure 1h and Figure S8. The corresponding shell-by-shell fitting data are presented in Table S8 and S9 with anisotropic Mn-O bond lengths of 1.870 and 1.971 Å for NLMT-0 and uniform Mn-O bond lengths of 1.902 Å for NLMT-8. This implies inhibition of Jahn–Teller effect and formation of symmetric MnO_6 octahedra in NLMT-8, induced by the reinforced Mn-O bonds with occupation of Li^+ in both TMO_2 and Na layers.

2.2. Electrochemical Performance

The electrochemical properties of the cathode materials are evaluated in Na cells between 1.8 and 4.3 V. Their charge/discharge profiles in selected cycles at 25 mA g^{-1} are depicted in Figure 2a and S9. NLMT-0, NLMT-5, NLMT-8, and NLMT-10 exhibit smoother charge/discharge curves, compared to P'2-NM. This suggests that introduction of Ti hinders Na^+/vacancy ordering during Na^+ (de)intercalation, in agreement with disappearance of several current peaks in cyclic voltammetry (CV) curves in Figure S10a and S10b.[16] The voltage plateau at 3.5 V diminishes with increased amounts of Li substitution, which is reflected in the gradual

disappearance of the current peak at 3.5 V in Figure S10c-S10e. This indicates that the phase transition of P'2↔OP4 is suppressed during charge.[17] The initial discharge capacities of P'2-NM, NLMT-0, NLMT-5, NLMT-8, and NLMT-10 materials are 195, 170, 165, 163 and155 $mAhg^{-1}$, corresponding to insertion of 0.75, 0.65, 0.63, 0.62 and 0.59 mol Na^+ per formula, respectively. Their cycling performances at 250 mA g^{-1} in Figure 2b present capacity retention of 5%, 32%, 85%, 90% and 88%, respectively, after 500 cycles, indicating superior cycling stability of NLMT-8.

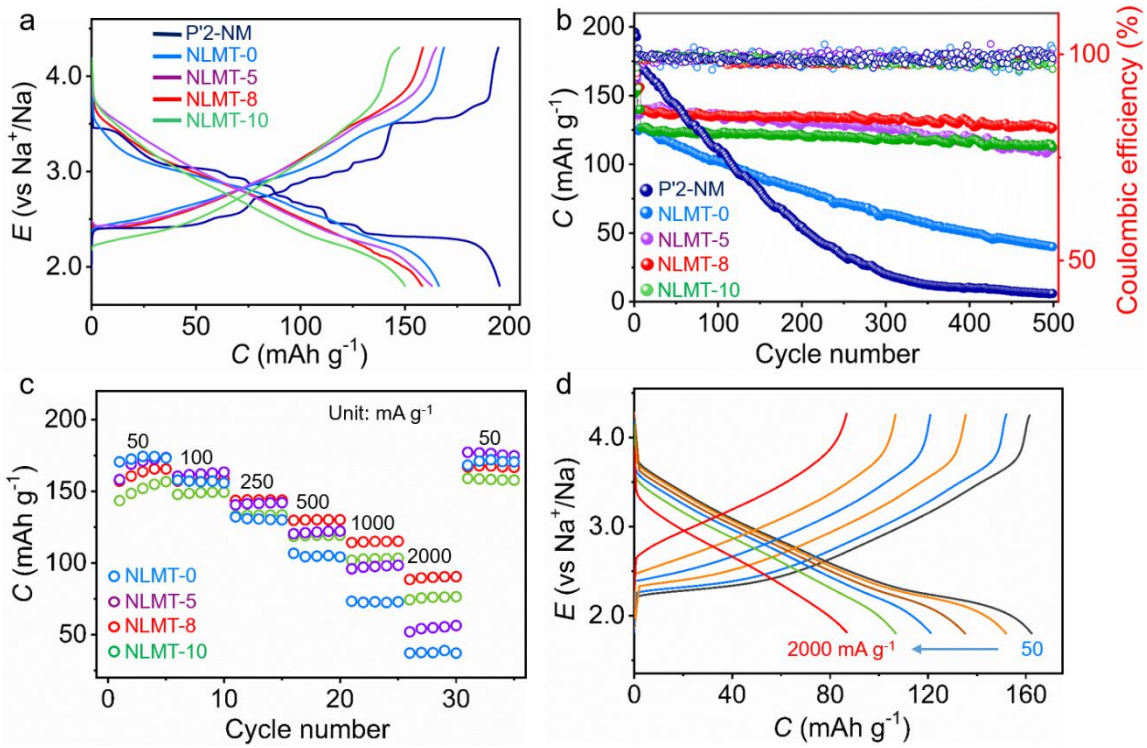

Figure 2. Electrochemical performances. (a) Charge/discharge curves of the 2nd cycle of P'2-NM, NLMT-0, NLMT-5, NLMT-8 and NLMT-10 at 25 mA g^{-1} between 1.8 and 4.3 V. (b) Cycling stability at 250 mA g^{-1}. (c) Rate capabilities at different current rates. (d) Selected charge/discharge curves of NLMT-8.

The rate performances of NLMT-*x* (*x* = 0, 5, 8 and 10) and P'2-NM are compared in Figure 2c and S11. The initial discharge capacity of NLMT-8 is 162 mAh g^{-1} at 50 mA g^{-1}. It can maintain 96%, 87%, 78%, 69% and 55% of the initial capacity as the discharge current is increased by 2, 5, 10, 20 and 40 fold, respectively. At 2000 mA g^{-1}, the delivered capacities of P'2-NM, NLMT-0, NLMT-5, NLMT-8 and NLMT-10 are 31, 37, 56, 89 and 76 $mAhg^{-1}$, respectively. This indicates the superior rate capability of NLMT-8. Selected galvanostatic charge/discharge curves of NLMT-8 at different currents are shown in Figure 2d. The improved cycling and rate performances of NLMT-8 are rewarded by its enhanced structure stability in hexagonal symmetry and facile Na^+ transport within the enlarged Na layers.

2.3. Structure Evolution

The structure evolution of NLMT-8 in the first cycle and second charge is examined by *in-situ* XRD between 14° and 70° at 20 mA g^{-1} in Figure 3a. The corresponding charge/discharge curves are depicted in Figure 3b. During the initial charge to 4.3 V, the (101), (102), and (103) diffraction peaks move toward higher angles because of the contracted *ab* plane, which is resulted from the smaller TM ion radius upon electrochemical oxidation. Meanwhile, the (002) and (004) peaks of NLMT-8 shift to lower angles, indicating the expanded *c* axis due to increased electrostatic repulsion between adjacent oxygen layers. Although some extent of peak broadening is observed after fully charged to 4.3V, peak position and profile can be resumed close to the original ones after discharged to 1.8 V, suggesting highly reversible Na^+ (de)intercalation behavior in NLMT-8. The absence of new peaks indicates a complete solid-solution reaction in NLMT-8 during desodiation and sodiation. The phase-transition-free process is further confirmed by HRTEM images at the state of 4.3 V-charge and and 1.8 V-discharge in Figure S12. NLMT-8 maintains the P2-type structure throughout the electrochemical cycles.

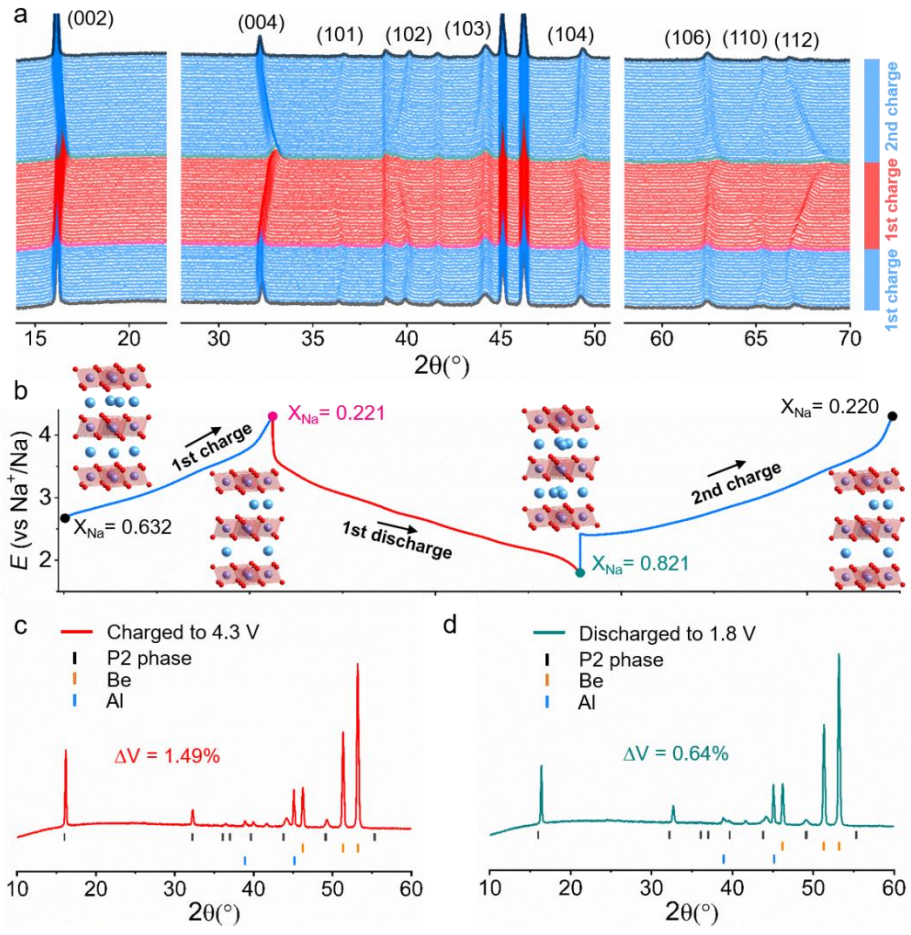

Figure 3. Structure evolution upon Na^+ (de)intercalation. (a) *In-situ* XRD patterns collected during the first charge/discharge and second charge of NLMT-8 at 20 mA g^{-1} between 1.8 and 4.3 V. (b) Schematic of structure evolution of NLMT-8. XRD patterns of NLMT-8 at the states of (c) 4.3 V-charge and (d) 1.8 V-discharge.

The solid-solution reaction is also evident in the continuous variation of lattice constants (*a* and *c*) and unit cell volume (V) of NLMT-8 at different charge/discharge states. As shown in Figure S13, the changes of *a* and *c* are consistent with the shift of the (*10l*) and (*00l*) diffraction peaks in the *in-situ* XRD patterns in Figure 3a. The variation in cell volume of NLMT-8 at the end of the first charge and discharge is 1.49% and 0.64%, respectively. The corresponding XRD patterns are depicted in Figure 3c and 3d and Figure S14 with their refined results in Table S10 and S11. Such low volume changes are nearly zero strain and benefited from the solid-solution pathway in NLMT-8.[18] This is distinctively contrast to the P'2↔OP4 and P'2↔P"2 phase transitions in P'2-NM and NLMT-0 in Figure S15-17, as the volume change for the major phase transition of P'2↔OP4 was reported to be 9%.[5a] These suggest that Li substitution effectively suppresses phase transitions in NLMT-8, which enhances its cycling stability and rate performance in Figure 2b and 2c.

2.4. Charge Compensation

Ex-situ X-ray absorption spectroscopy (XAS) measurements are carried out to elucidate the charge compensation of NLMT-8 upon desodiation and sodiation. The XANES spectra at the Mn K-edges are collected at different charge/discharge states with their corresponding Fourier-transformed extended X-ray absorption fine structure (EXAFS) analyses in Figure 4a and 4b, respectively. During the initial charge to 4.3 V, the Mn absorption edge moves to a higher energy region, approaching the MnO_2 reference, indicating oxidation of Mn^{3+} to Mn^{4+}. This is confirmed by the half-height method according to the half-edge energy ($E_{0.5}$) at the Mn K-edges in Figure S18,[19] which indicates that the charge of NLMT-8 proceeds with oxidation of $Mn^{3.45+}$ to $Mn^{3.87+}$. This is consistent with the shortened interatomic distance in the first Mn-O and second Mn-TMs coordination shells in Figure 4b. Ti is shown to have no electrochemical activity by X-ray photoelectron spectroscopy (XPS) in Figure S19. The EXAFS fittings in Table S12 show that the Mn–O bond length and Mn-TMs distance decrease from 1.906 and 2.913 Å to 1.902 and 2.898 Å, respectively, upon charging to 4.3 V. The negligible bond length variations are in good agreement with the small volume change of 1.49% in Figure 3c for NLMT-8.

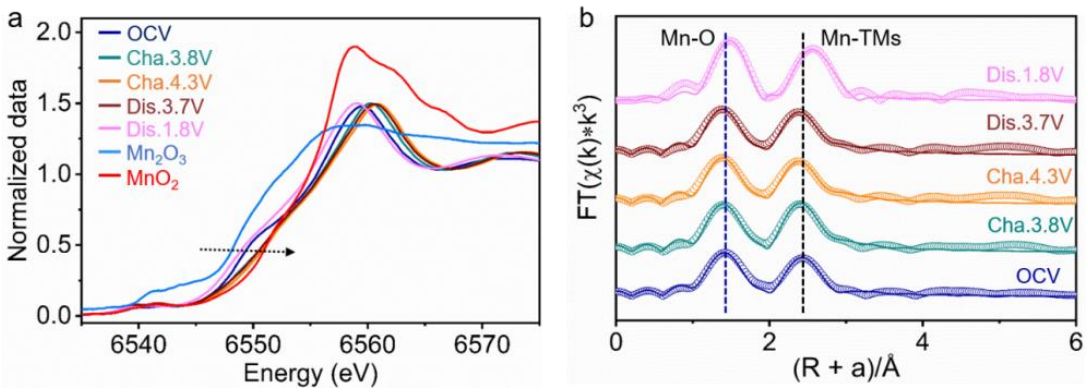

Figure 4. Charge compensation of NLMT-8 upon desodiation and sodiation. (a) *Ex-situ* XANES spectra at the Mn K-edges collected at different charge/discharge states. (b) Corresponding Fourier-transformed EXAFS spectra at the Mn K-edges.

2.5. Insights from First-Principles Calculations

Density functional theory (DFT) calculations with Vienna Ab-initio Simulation Package (VASP) were performed to identify the critical role of Li in NLMT-8.[20] Given the results in Figure 1f that Li^+ predominantly sits in the TMO_2 slabs, the optimized structure of NLMT-8 is shown in Figure S20. Figure 5a shows the molecular dynamics simulations of NLMT-8 at 800K, in which the mean square displacements (MSDs) indicate the diffusion capability of each element from 0 to 10 ps. It is clear that the Na^+ diffusion is much easier than the other elements, and Li^+ is nearly immobile as simulation time increases. This is consistent with the ICP-OES results in Table S13, in which the content of Li^+ in both the TMO_2 slabs and Na layers remains almost invariant after 50 charge/discharge cycles, suggesting negligible Li^+ loss in NLMT-8 upon desodiation and sodiation.

Bader charge analysis is used to disclose the effect of Li substitution on the structure of NLMT-8 in Figure 5b and 5c. The average charge around the O atoms in LiO_6 octahedron is -1.04, which is less negative than -1.07 of MnO_6 and -1.21 of TiO_6 octahedra. This implies high ionicity of Li–O bonds and high covalency of Ti-O bonds.[15] The charge density analysis of NLMT-0 and NLMT-8 in Figure 5d shows that Ti-O bonds can effectively reduce the electrostatic attraction between Na and O, as shown in the red square region. This leads to a larger Na layer spacing in NLMT-0 than in P'2-NM (Table S7). In addition, the ionic Li-O bond induces additional electrons around the O atoms. This is in good agreement with the Bader charge analysis in Figure 5c. More electrons around O lead to strong electron cloud overlap between Mn and O, which is evidenced by the right-shifted Mn K-edge of NLMT-8 in Figure 1g, thus reinforcing the covalency of Mn-O bonds and improving its structure stability.

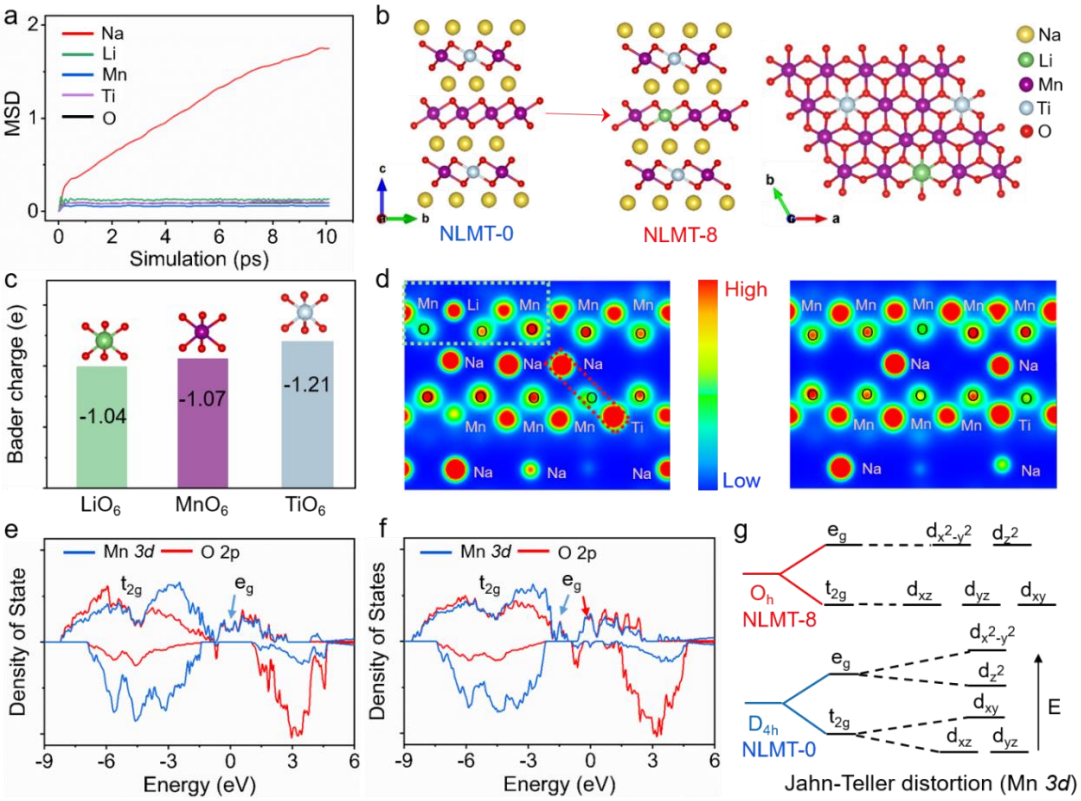

Figure 5. Simulated atomic and electronic structures. (a) MSDs of Na, Li, Mn, Ti and O as functions of time in NLMT-8 at 800K. (b) Schematic structures of NLMT-0 and NLMT-8. (c) Average Bader charge of O atoms in MO_6 octahedron (M = Li/Mn/Ti). (d) Contour maps of charge density on the (100) plane in NLMT-8 and NLMT-0. pDOS of (e) NLMT-8 and (f) NLMT-0. (g) Schematic illustration of Mn *3d* orbitals for NLMT-0 and NLMT-8.

The partial density of states (pDOS) of NLMT-8 and NLMT-0 is calculated by DFT calculations. In Figure 5e, the Mn *3d* orbitals of NLMT-8 split into two sets, namely, the degenerate t_{2g} (d_{xz}, d_{yz}, d_{xy}) and e_g (d_z^2 and d_x^2-$_y^2$) orbitals. It is shown that Mn is more prone to electron donation and being oxidized according to the mainly attribution of Mn e_g orbital to the valence band.[21] The degenerate e_g orbitals suggest the mitigated Jahn-Teller effect and uniform Mn-O bond lengths of MnO_6 octahedra, which are consistent with the EXAFS spectra of NLMT-8 in Figure 1h and Table S9. This is contrast to the pDOS of NLMT-0 in Figure 5f, where e_g orbitals split into two pairs with occupied d_z^2 and unoccupied d_x^2-$_y^2$ orbitals under and above the Fermi energy level, respectively. The non-degenerate e_g orbitals result in anisotropic Mn-O bond lengths and strong Jahn-Teller distortion of MnO_6 octahedra, as confirmed in Figure S8 and Table S8. These lead to O_h and D_{4h} symmetries of Mn *3d* orbitals for NLMT-8 and NLMT-0 in Figure 5g, respectively.[8] D_{4h} symmetry deforms the MnO_6 octahedra of NLMT-0 to an orthorhombic structure. The O_h symmetry benefited from the degenerate e_g orbitals gives rise to the symmetric MnO_6 octahedra. which facilitates formation of hexagonal

structure of NLMT-8. Its high symmetry hinders gliding of TMO_2 slabs upon Na^+ extraction/insertion, thus suppressing phase transitions of NLMT-8 in Figure 3a.

2.6. Na^+ Kinetics and Full Cell Performance

Galvanostatic intermittent titration (GITT) measurements are performed to estimate Na^+ diffusion coefficients (D_{Na}+) in P'2-NM and NLMT-x (x=0, 5, 8 and 10) in the second cycle in Figure 6a and S21. D_{Na}+ of P'2-NM NLMT-0, NLMT-5, NLMT-8 and NLMT-10 is calculated to be 10^{-11}, 2×10^{-11}, 3×10^{-11}, 4×10^{-11} and 2×10^{-11} cm^2 s^{-1} in Figure 6b, and Figure S22 and S23, respectively. The high D_{Na}+ of NLMT-8 is in good agreement with its larger Na layer spacing in Tables S7. The equilibrium voltage of NLMT-8 shows a continuous change, suggesting its solid-solution reaction process during Na^+ (de)intercalation.[22] In order to determine the role of the symmetry change from an orthorhombic to hexagonal structure induced by Li substitution, the energy difference between the edge-sharing (Na_e) and face-sharing (Na_f) sites is calculated and depicted in Figure 6c. It is reduced from 336 meV in NLMT-0 to 128 meV in NLMT-8, and indicates that the structure with hexagonal symmetry effectively reduces the energy difference between Na_e and Na_f. This can avoid formation of ordered intermediate phases and allow the complete solid-solution reaction in NLMT-8 in Figure 3a.[12]

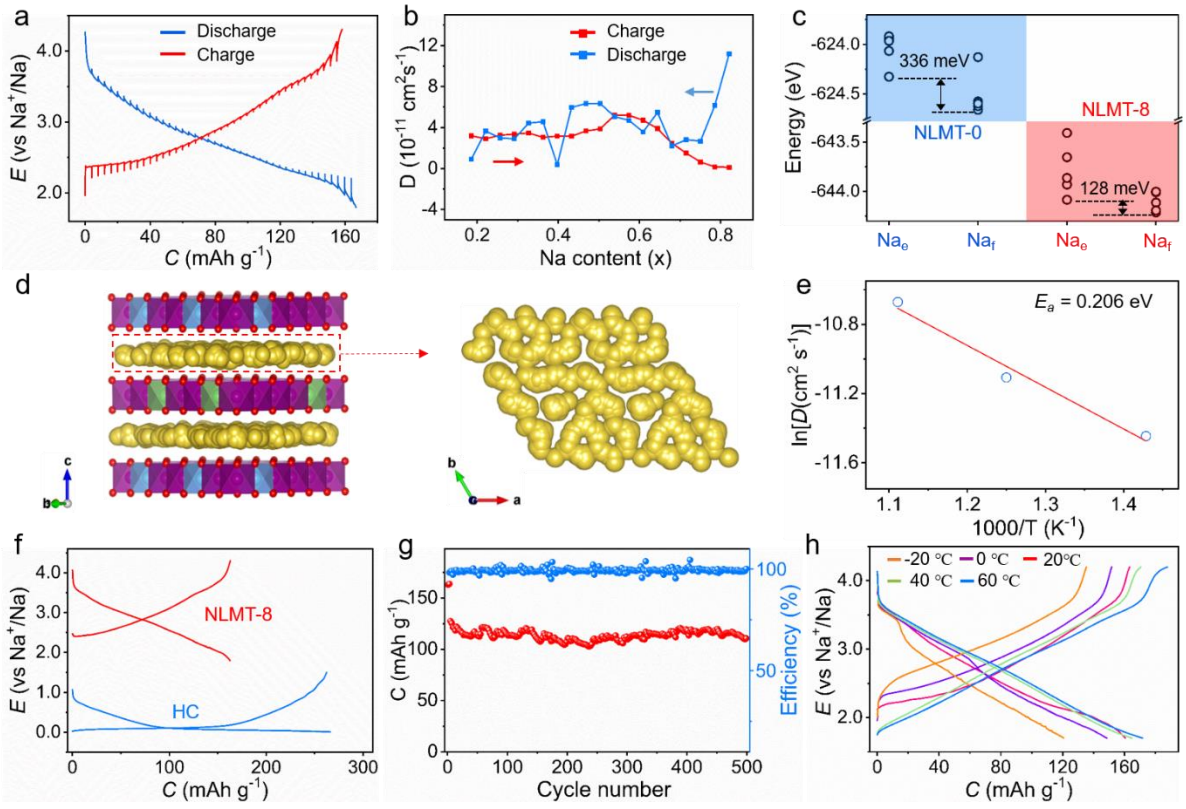

Figure 6. Na^+ kinetics and full cell performance. (a) GITT charge/discharge curves of NLMT-8. (b) Calculated Na^+ diffusion coefficients of NLMT-8. (c) Energy difference between Na_e and Na_f sites in NLMT-0 and NMLT-8. (d) Trajectories of Na^+ in NLMT-8. (e) Arrhenius plot of Na^+ diffusion coefficients in NLMT-8. (f) Charge/discharge profiles at the first cycle of NLMT-8 and HC at 25 mA g^{-1}. (g) Cycling performance of HC//NLMT-8 full cell between 1.7 and 4.2 V at 250 mA g^{-1}. (h) Charge/discharge profiles of full cell at -20 °C ~60 °C at 25 mA g^{-1}.

Ab initio molecular dynamics (AIMD) simulations are carried out at the temperatures from 700 to 900 K to investigate Na^+ transport in NLMT-8. Figure 6d and S24 show the trajectories of Na^+ in NLMT-8 from the AIMD simulations. Na^+ migrates through two-dimensional pathways, featuring as interconnected diffusion channels. The corresponding top view of trajectories within a Na layer is presented on the right-hand side of Figure 6d. It shows an ideal Na_f-Na_e-Na_f diffusion pathway and agrees well with the small energy difference between the Na_f and Na_e sites in Figure 6c.[23] The slopes of MSDs at different temperatures in Figure 3a and S25 are fitted to obtain the diffusion coefficient (D) of NLMT-8 in Figure 6e. The diffusion energy barrier (E_a) is calculated to be 0.206 eV based on the slope of Arrhenius plot, which is very low and consistent with the good rate performance of NLMT-8 in Figure 2c.

A full cell with NLMT-8 as the cathode and hard carbon (HC) as the anode is constructed in Figure S26a. HC anode is presodiated by discharging to 0.01 V in a Na cell at 25 mA g^{-1} and then extracted in a glove box. The typical charge/discharge curves of NLMT-8 and HC, as well as the full cell, are shown in Figure 6f and S26b. The full cell delivers a reversible capacity of 165 mAh g^{-1} at 25 mA g^{-1} and 128 mAh g^{-1} at 250 mA g^{-1} based on the mass of cathode material. It exhibits excellent cycling stability with capacity retention of 88.2% over 500 cycles in Figure 6g. It also exhibits good electrochemical performance at different temperatures in Figure 6h. The discharge capacity increases from 120.5 to 171.2 mAh g^{-1} as the temperature increases from -20 °C to 60 °C. The efficient Na^+ storage over a wide temperature range depends on the favorable Na^+ diffusion in NLMT-8, suggesting its promising application for high-performance SIBs.

3. Conclusion

In summary, a new cathode material of NLMT-8 has been synthesized with Li and Ti incorporated into the TMO_2 layers. The high covalency of Ti-O bonds effectively enlarges the Na layer spacing and suppresses Na^+/vacancy rearrangements by reducing the electrostatic interaction between Na and O. Highly ionic nature of the Li-O bonds reinforces the covalency of the Mn-O bonds, leading to the degenerate Mn $d_{x^2-y^2}$ and d_{z^2} orbitals and symmetric MnO_6 octahedra. This effectively eliminates the Jahn-Teller effect and induces crystal symmetry

change from the orthorhombic to more stable hexagonal structures. A complete solid-solution reaction in NLMT-8 is revealed by *in-situ* XRD, which is contrast to the typical two-phase reactions of P'2↔OP4 and P'2↔P"2 in both the high and low voltage regions of P'2-NM and NLMT-0. The mitigated phase transition leads to smooth charge and discharge curves without any voltage plateaus, ultra-stable cycling performance (90.2% capacity retention after 500 cycles), and good rate capability (95.5 mAh g^{-1} at 2000 mA g^{-1}). These may provide insights into the rational design of cathode materials with low electronegativity dopants to modulate the electron population of Mn *3d* orbitals and hence avoid the Jahn-Teller distortion for a robust host for Na^+ storage.

4. Experimental Section

Materials Synthesis: All chemicals are analytically pure without further purification, and were purchased from Alfa Aesar. The precursor of NLMT-8 was synthesized via a solid-state method. Typically, stoichiometric amounts of Na_2CO_3 (5 mol% in excess), Li_2CO_3, Mn_2O_3 and TiO_2 were mixed in a ball mill tank with acetone for 6 h at 400 rpm to ensure complete mixing. The as-synthesized precursor was dried at 80 °C for 12 h and then pressed into pellet under 20 MPa. The pellet was annealed in a muffle furnace at a rate of 5 °C min^{-1} from room temperature to 1000 °C for 15 h, then quenched and immediately transferred into an argon-filled glove box to avoid structure damage from the moisture in air. Similar processes were utilized for the synthesis of P′2-NM, NLMT-0, NLMT-5 and NLMT-10.

Materials Characterization: The chemical compositions were determined by ICP analysis (ICP-OES, SPECTRO-BLUE). XRD patterns were collected from a Rigaku Smart Lab equipped with a Cu Kα radiation source. Rietveld refinement was conducted using the Fullprof software.[24] *Ex-situ* XAS at the Mn K-edges were collected at Argonne National Laboratory (9700 South Cass Avenue, Lemont, IL 60439 USA). XAS data was collected in fluorescence mode and processed by Demeter software package.[25] . ^{7}Li magic-angle spinning (MAS) NMR experiments were performed on JNM-ECZ600R in a 14.1 T magnetic field with a 7Li Larmor frequency of 194.34 MHz. Electrodes were packed into 2.5 mm rotors and spun at a MAS rate of 30 kHz. The EXAFS region was k^3-weighted and Fourier transformed in the k range of 2.5-10.0 $Å^{-1}$. A schematic structure of the sample was illustrated by VESTA software.[24b] The morphology of samples was detected by SEM (JEOL JSM-7900F, AEMC, 5 kV). HRTEM images and EDS mappings were captured by TEM (FEI Talos F200X G2, AEMC, 200 kV). EELS measurements, HAADF- and ABF-STEM images were captured on a JEM-ARM200F (AEMC) with an accelerating voltage of 200 kV.

Electrochemical Measurements: Coin cells (CR2032) were assembled in an argon-filled glove box for all electrochemical tests. The electrode slurry was composed of active material (80 wt%), Super P (10 wt%), and polyvinylidene fluoride (10 wt%) in N-methyl-2-pyrrolidone, and then coated onto an aluminum foil and dried in a vacuum at 100 °C for 10 h. The loading of active material in each electrode pellet of 10.0 mm diameter is ~3.5 mg cm^{-2}. Sodium foil was used as the anode, 1.0 M $NaPF_6$ in dimethyl carbonate (DMC): propylene carbonate (PC) (1:1) with addition of 2 wt% fluoroethylene carbonate (FEC) as the electrolyte, and glass fiber filter papers act as the separator. Electrochemical cycles and GITT were carried out on a Land CT2001A battery test system (Land, Wuhan, China) in a voltage range of 1.8-4.3 V at 25°C. GITT was conducted by repeatedly applying current pulse 10 mA g^{-1} for 0.5 h and then relaxation for 4 h. CV tests were performed on a Solartron 1470E electrochemical workstation with a voltage range of 1.8-4.3 V at 0.1 mV s^{-1}. The full cell was assembled with NLMT-8 as the cathode and hard carbon (HC) as the anode. The HC was presodiated by discharging it to 0.01 V at 50 mA g^{-1} in a Na cell. The mass ratio of NLMT-8/HC is around 1.2, corresponding to 10% anode capacity in excess. The charge and discharge of full cells were performed from -20°C to 60°C within 1.7-4.2 V.

DFT Calculations: DFT calculations were performed using Vienna ab-initio simulation package (VASP) with the generalized gradient approximation plus U (GGA+U) and the Perdew-Burke-Eznerhof (PBE) functional (GGA-PBE) to describe the exchange-correlation energy of electrons.[20, 26] The U values of Mn are set as 4.0 eV. The projector-augmented wave method (PAW) was used to treat the interaction between the atomic cores and electrons.[27] Ab-initio molecular dynamic (AIMD) simulation was performed to determine Na^+ diffusion at 700, 800 and 900 K using the canonical (NVT) ensemble each for 10 ps with 1 fs time steps.[28] A 6×4×4 K-point mesh was used to construct the reciprocal space, and a cutoff of 400 eV was applied in both optimization and AIMD calculations. During Bader analyses, the cutoff energy was increased to 450 eV for higher precision, and a 8×4×6 K-point matrix was adopted. Atomic positions and cell parameters were fully optimized until all force components were less than 0.02 eV $Å^{-1}$. All visualization of structures was presented using VESTA.

Supporting Information

Supporting Information is available from the Wiley Online Library or from the author.

Acknowledgements

This work was supported by the National Natural Science Foundation of China (Grant No. 52171215 and 21835004), Tianjin Natural Science Foundation (Grant No. 19JCJQJC62400), and Haihe Laboratory of Sustainable Chemical Transformations. This research used resources of the Analysis Platform of New Matter Structure at Nankai University. Research at Argonne National Laboratory was supported by the U.S. Department of Energy (DOE), Office of Energy Efficiency and Renewable Energy. Argonne National Laboratory is operated for the DOE Office of Science by UChicago Argonne, LLC, under Contract DE-AC02-06CH11357.

Received: ((will be filled in by the editorial staff))
Revised: ((will be filled in by the editorial staff))
Published online: ((will be filled in by the editorial staff))

References

[1] a) A. Van der Ven, Z. Deng, S. Banerjee, S. P. Ong, *Chem. Rev.* **2020**, *120*, 6977-7019; b) J.-Y. Hwang, S.-T. Myung Y.-K. Sun, *Chem. Soc. Rev.* **2017**, *46*, 3529-3614.

[2] a) W. Zuo, J. Qiu, X. Liu, F. Ren, H. Liu, H. He, C. Luo, J. Li, G. F. Ortiz, H. Duan, J. Liu, M. Wang, Y. Li, R. Fu, Y. Yang, *Nat. Commun.* **2020**, *11*, 3544; b) Y. Liang, H. Dong, D. Aurbach, Y. Yao, *Nat. Energy* **2020**, *5*, 646-656.

[3] a) C. Zhao, Q. Wang, Z. Yao, J. Wang, B. Sánchez-Lengeling, F. Ding, X. Qi, Y. Lu, X. Bai, B. Li, H. Li, A. Aspuru-Guzik, X. Huang, C. Delmas, M. Wagemaker, L. Chen, Y. Hu, *Science* **2020**, *370*, 708; b) K. Kubota, S. Komaba, *J. Electrochem. Soc.* **2015**, *162*, A2538-A2550.

[4] a) X. Liu, W. Zuo, B. Zheng, Y. Xiang, K. Zhou, Z. Xiao, P. Shan, J. Shi, Q. Li, G. Zhong, R. Fu, Y. Yang, *Angew. Chem. Int. Ed.* **2019**, *58*, 18086-18095; b) M. Ren, H. Fang, C. Wang, H. Li, F. Li, *Energy & Fuels* **2020**, *34*, 13412-13426.

[5] a) S. Kumakura, Y. Tahara, K. Kubota, K. Chihara, S. Komaba, *Angew. Chem. Int. Ed.* **2016**, *55*, 12760-12763; b) Y. Zhu, Y. Xiao, S. Dou, Y. Kang, S. Chou, *eScience* **2021**, *1*, 13-27.

[6] J. U. Choi, J. H. Jo, Y. J. Park, K. S. Lee, S. T. Myung, *Adv. Energy Mater*. **2020**, *10*, 2001346.

[7] a) S. Kumakura, Y. Tahara, S. Sato, K. Kubota S. Komaba, *Chem. Mater.* **2017**, *29*, 8958-8962; b) M. Ren, S. Zhao, S. Gao, T. Zhang, M. Hou, W. Zhang, K. Feng, J. Zhong, W. Hua, S. Indris, K. Zhang, J. Chen, F. Li, *J. Am. Chem. Soc*. **2022**, *145*, 224-233.

[8] P.-F. Wang, T. Jin, J. Zhang, Q.-C. Wang, X. Ji, C. Cui, N. Piao, S. Liu, J. Xu, X.-Q. Yang C. Wang, *Nano Energy* **2020**, *77*, 105167.

[9] a) Y. J. Park, J. U. Choi, J. H. Jo, C.-H. Jo, J. Kim, S.-T. Myung, *Adv. Funct. Mater.* **2019**, *29*, 1901912; b) C. Wang, L. Liu, S. Zhao, Y. Liu, Y. Yang, H. Yu, S. Lee, G.-H. Lee, Y.-M. Kang, R. Liu, F. Li, J. Chen, *Nat. Commun.* **2021**, *12*, 2256.

[10] J. Xu, D. H. Lee, R. J. Clément, X. Yu, M. Leskes, A. J. Pell, G. Pintacuda, X.-Q. Yang, C. P. Grey Y. S. Meng, *Chem. Mater.* **2014**, *26*, 1260-1269.

[11] a) S.-M. Oh, S.-T. Myung, J.-Y. Hwang, B. Scrosati, K. Amine, Y.-K. Sun, *Chem. Mater.* **2014**, *26*, 6165-6171; b) Y. You, S. Xin, H. Y. Asl, W. Li, P. Wang, Y. Guo A. Manthiram, *Chem* **2018**, *4*, 2124-2139.

[12] P. F. Wang, H. R. Yao, X. Y. Liu, Y. X. Yin, J. N. Zhang, Y. Wen, X. Yu, L. Gu Y. G. Guo, *Sci. Adv.* **2018**, *4*, eaar6018.

[13] Y. Liu, C. Wang, S. Zhao, L. Zhang, K. Zhang, F. Li J. Chen, *Chem. Sci.* **2021**, *12*, 1062-1067.

[14] W. Zhang, D.-H. Seo, T. Chen, L. Wu, M. Topsakal, Y. Zhu, D. Lu, G. Ceder F. Wang, *Science* **2020**, *367*, 1030.

[15] L. Yang, X. Li, J. Liu, S. Xiong, X. Ma, P. Liu, J. Bai, W. Xu, Y. Tang, Y.-Y. Hu, M. Liu H. Chen, *J. Am. Chem. Soc.* **2019**, *141*, 6680-6689.

[16] Y. Xie, E. Gabriel, L. Fan, I. Hwang, X. Li, H. Zhu, Y. Ren, C. Sun, J. Pipkin, M. Dustin, M. Li, Z. Chen, E. Lee H. Xiong, *Chem. Mater.* **2021**, *33*, 4445-4455.

[17] Y. Ling, J. Zhou, S. Guo, H. Fu, Y. Zhou, G. Fang, L. Wang, B. Lu, X. Cao S. Liang, *ACS Appl. Mater. Interfaces* **2021**, *13*, 58665-58673.

[18] T. Jin, P. F. Wang, Q. C. Wang, K. Zhu, T. Deng, J. Zhang, W. Zhang, X. Q. Yang, L. Jiao C. Wang, *Angew. Chem. Int. Ed.* **2020**, *59*, 14511-14516.

[19] H. Dau, P. Liebisch M. Haumann, *Anal Bioanal Chem.* **2003**, *376*, 562-583.

[20] G. Kresse J. Furthmüller, *Comput. Mater. Sci.* **1996**, *6*, 15-50.

[21] N. Yabuuchi, M. Takeuchi, M. Nakayama, H. Shiiba, M. Ogawa, K. Nakayama, T. Ohta, D. Endo, T. Ozaki, T. Inamasu, K. Sato S. Komaba, *Proc. Natl. Acad. Sci.* **2015**, *112*, 7650-7655.

[22] L. Yang, L.-Y. Kuo, J. M. López del Amo, P. K. Nayak, K. A. Mazzio, S. Maletti, D. Mikhailova, L. Giebeler, P. Kaghazchi, T. Rojo P. Adelhelm, *Adv. Funct. Mater.* **2021**, *31*, 2102939.

[23] S. Li, Y. Zhang, K. Lei, Q. Yang, Z. Liu, K. Jiang, F. Li, Q. Lu, D. Mikhailova S. Zheng, *J. Mater. Chem. A* **2022**, *10*, 10391-10399.

[24] a) J. Rodriguez-Carvajal, *IUCr Newsl.* **2001**, *26*; b) K. Momma, F. Izumi, *J. Appl. Crystallogr.* **2011**, *44*, 1272-1276..

[25] B. Ravel M. Newville, *J. Synchrotron. Radiat.* **2005**, *12*, 537-541.

[26] a) G. Kresse, J. Furthmüller, *Phys. Rev. B* **1996**, *54*, 11169-11186; b) S. L. Dudarev, G. A. Botton, S. Y. Savrasov, C. Humphreys, A. P. Sutton, *Phys. Rev. B* **1998**, *57*, 1505.

[27] J. P. Perdew, K. Burke M. Ernzerhof, *Phys. Rev. Lett.* **1996**, *77*, 3865-3868.

[28] R. Car M. Parrinello, *Phys. Rev. Lett.* **1985**, *55*, 2471-2474.

A whole-voltage-range solid-solution reaction is reported in P2-$Na_{0.643}Li_{0.078}Mn_{0.827}Ti_{0.095}O_2$ during (de)intercalation, in which Li in transition-metal and Na layers enhances covalency of Mn-O bonds for Mn 3*d* e_g orbital degeneracy to favor its hexagonal phase, and Ti-O bonds reduces the Na and O interaction for suppressed Na^+/vacancy rearrangements. This rewards its excellent cycling stability and rate capability.

Meng Ren, Zhuo Zhu, Zhaohui Liang, Yaohui Huang, Tong Zhang, Machuan Hou, Kai Zhang, Zonghai Chen, Yushi He, Zifeng Ma, Jun Chen and Fujun Li*

Whole-Voltage-Range Solid-Solution Reaction in Layered Oxide Cathode of Sodium-Ion Batteries

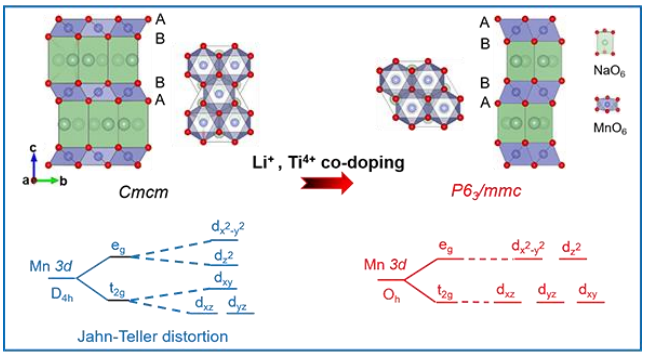

Supporting Information

Whole-Voltage-Range Solid-Solution Reaction in Layered Oxide Cathode of Sodium-Ion Batteries

*Meng Ren, Zhuo Zhu, Zhaohui Liang, Yaohui Huang, Tong Zhang, Machuan Hou, Kai Zhang, Zonghai Chen, Yushi He, Zifeng Ma, Jun Chen and Fujun Li**

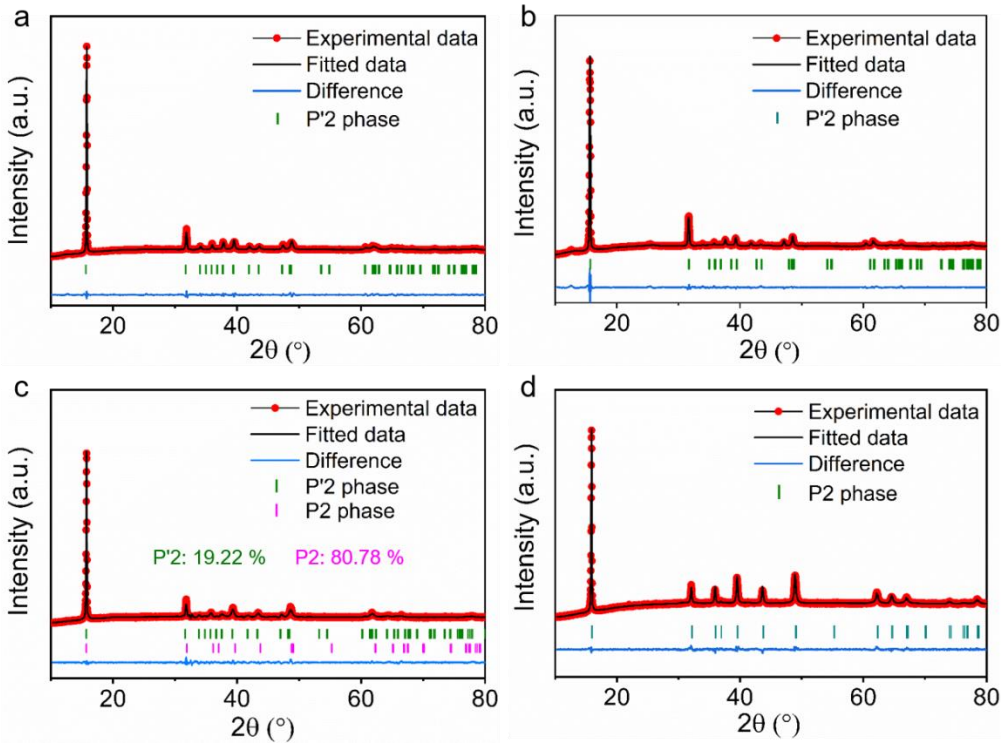

Figure S1. XRD Rietveld refinement for (a) P'2-NM, (b) NLMT-0, (c) NLMT-5, (d) NLMT-10.

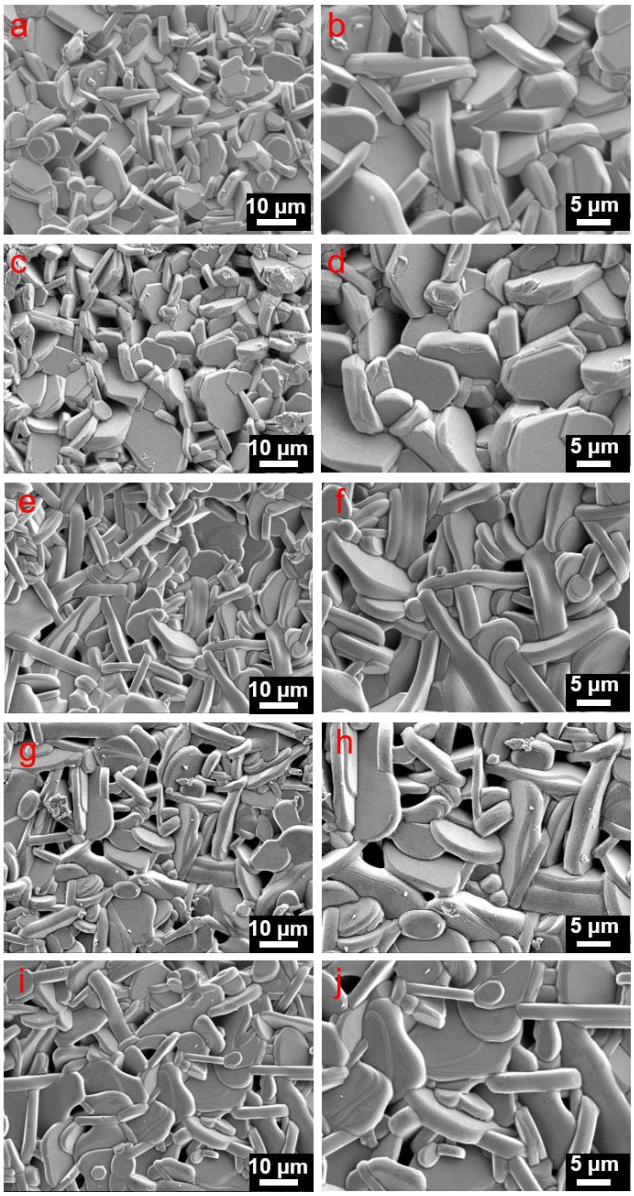

Figure S2. SEM images of (a, b) P'2-NM, (c, d) NLMT-0, (e, f) NLMT-5, (g, h) NLMT-8 and (i, j) NLMT-10.

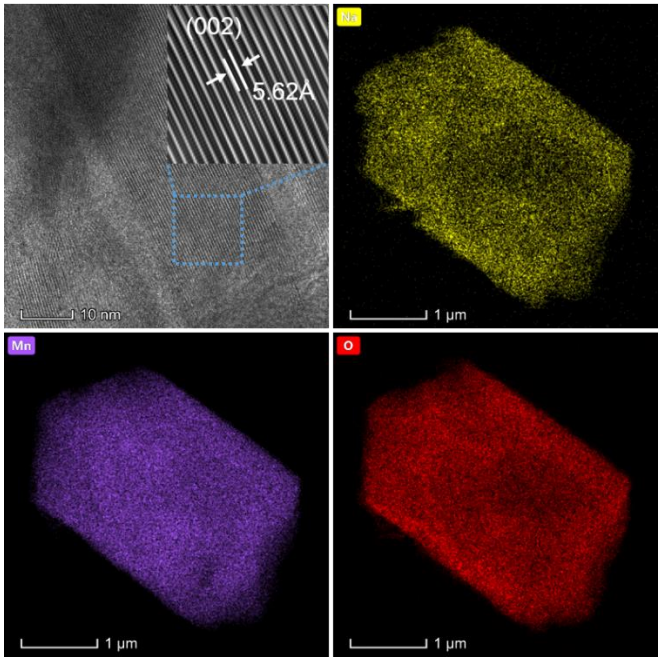

Figure S3. HRTEM figures and elemental mappings of P'2-NM.

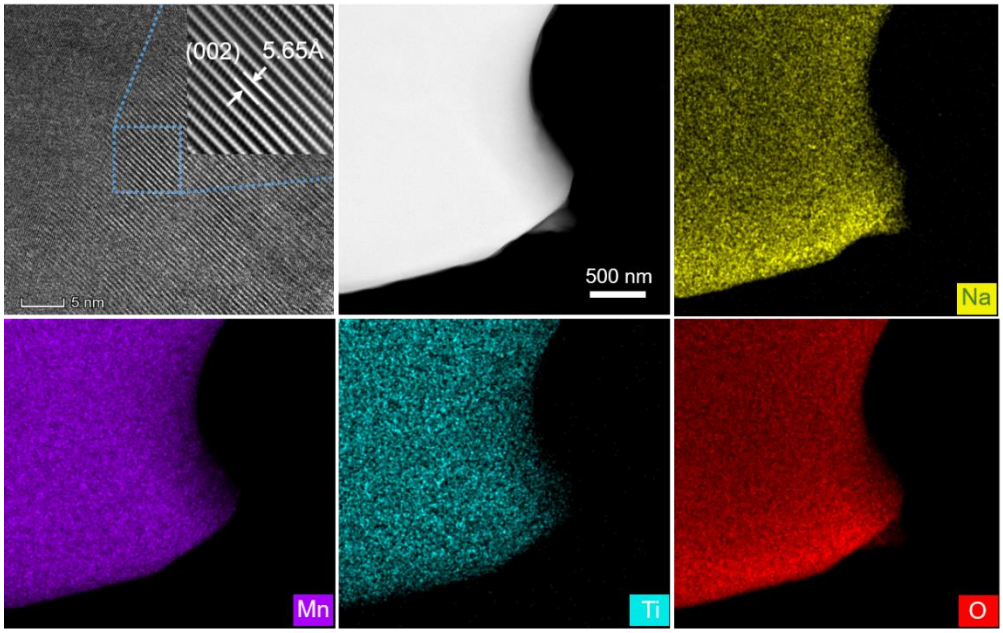

Figure S4. HRTEM figures and elemental mappings of NLMT-0.

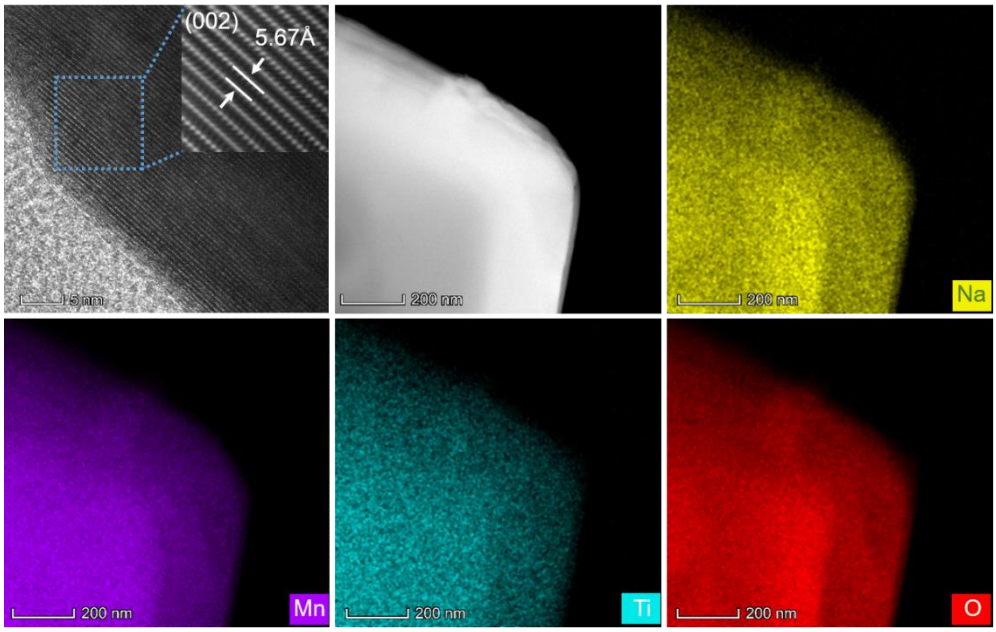

Figure S5. HRTEM figures and elemental mappings of NLMT-8.

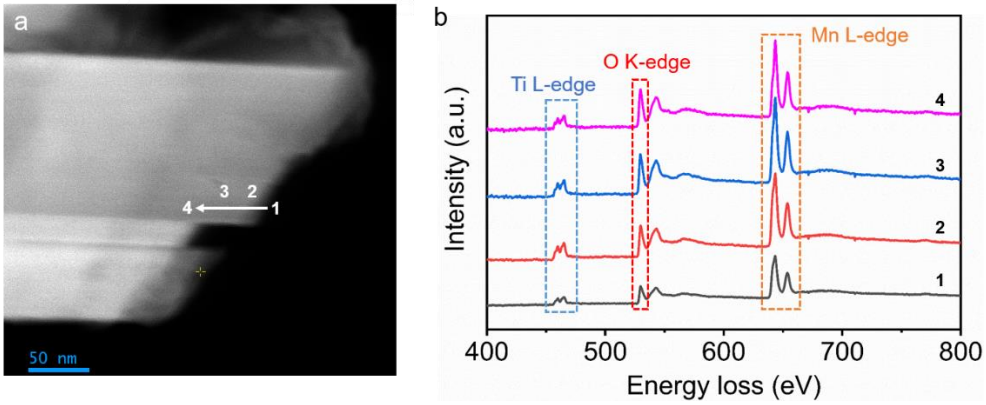

Figure S6. (a) HADDF-STEM image and (b) EELS spectra of NLMT-8.

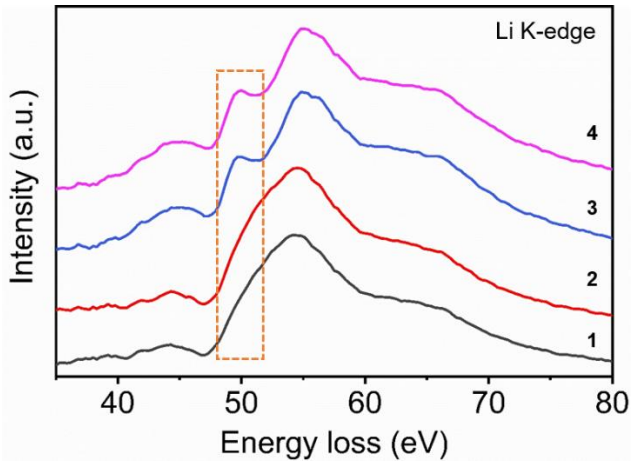

Figure S7. EELS spectra of NLMT-8.

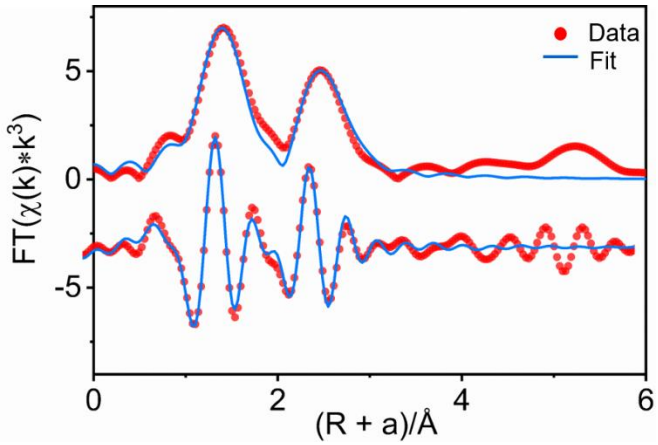

Figure S8. EXAFS at the Mn K-edge and curvefit for NLMT-0 shown in *R*-space (FT magnitude and imaginary component).

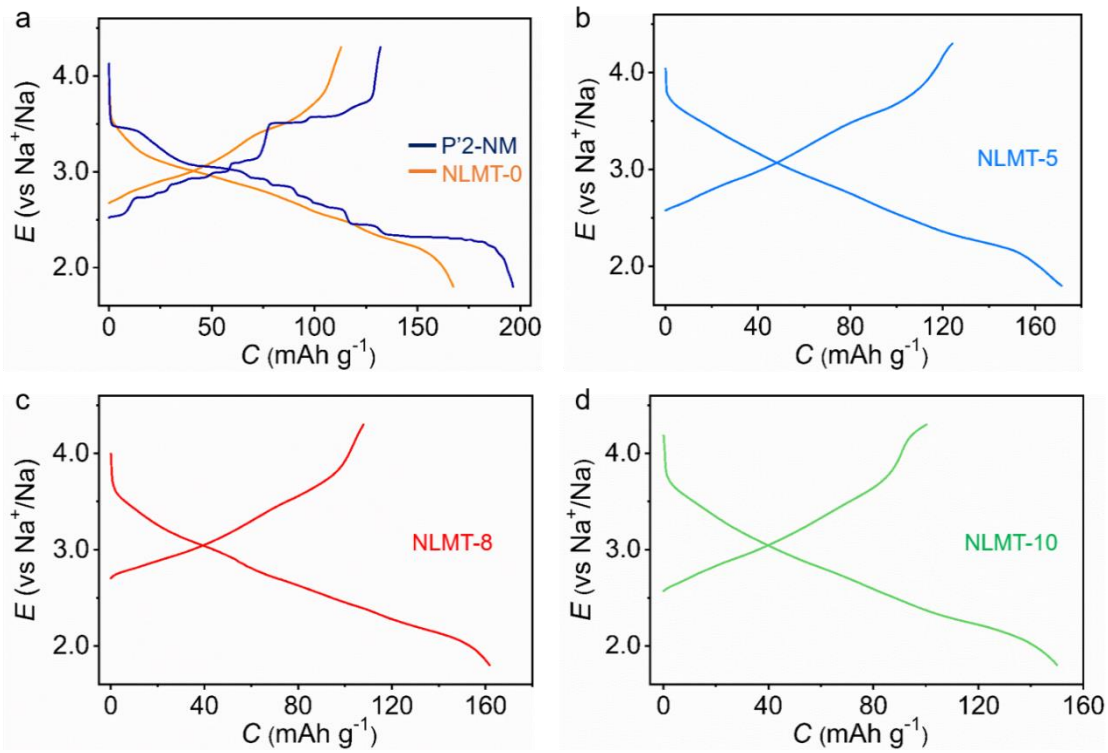

Figure S9. Charge/discharge curves of the 1st cycle at 25 mA g^{-1}.

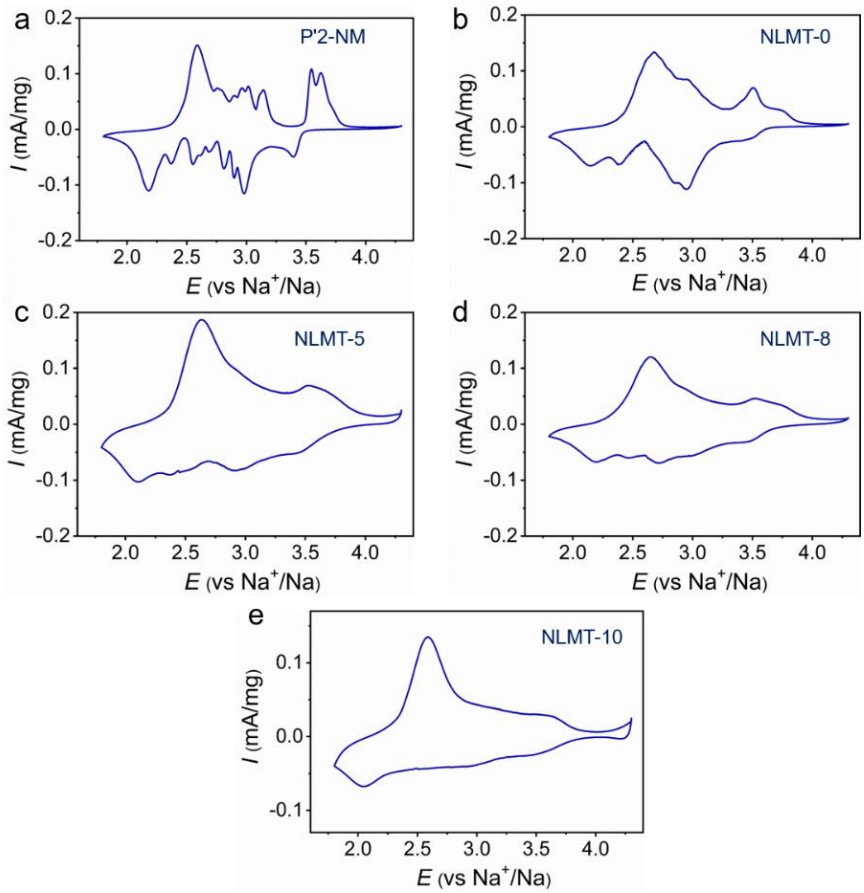

Figure S10. CV curves of the 2nd cycle at 0.1 mV s^{-1}.

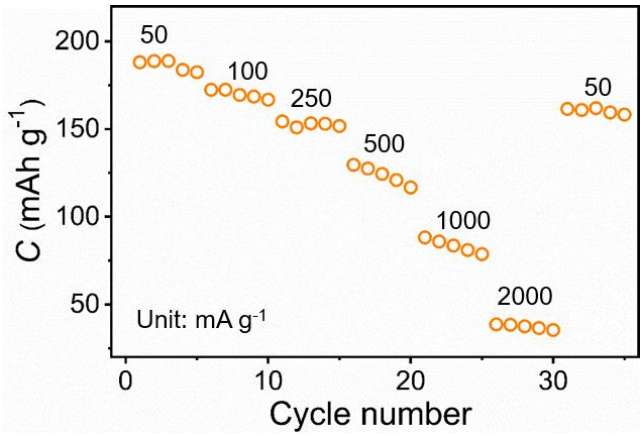

Figure S11. rate capability at varied rates of P'2-NM.

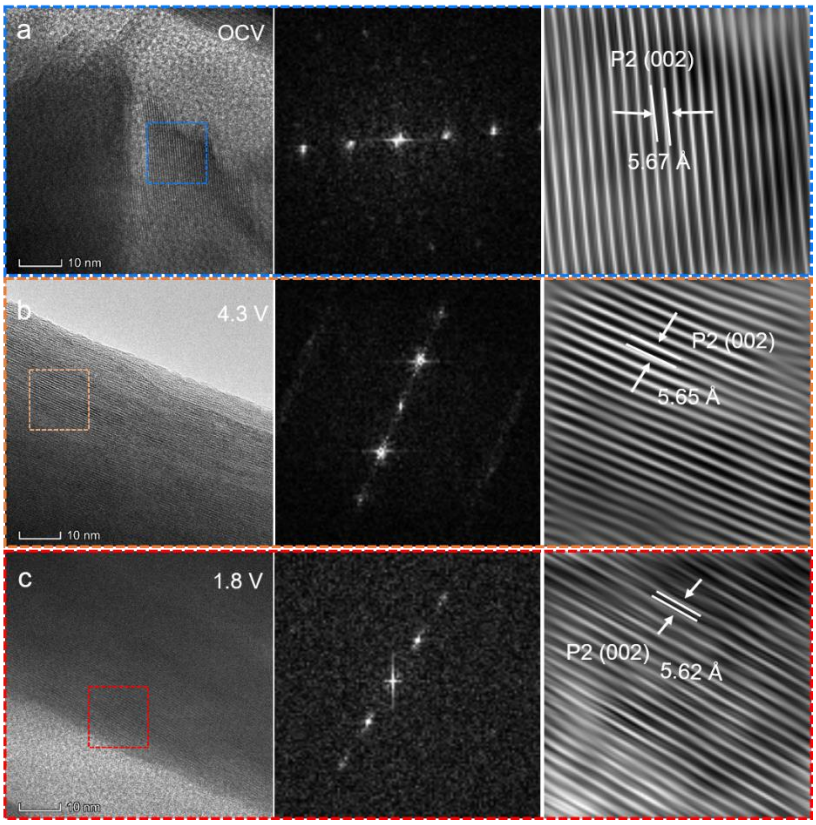

Figure S12. HRTEM images and corresponding FFT and inverse-FFT images of NLMT-8 at the states of (a) OCV, (b) 4.3 V-charge and (c) 1.8 V-discharge.

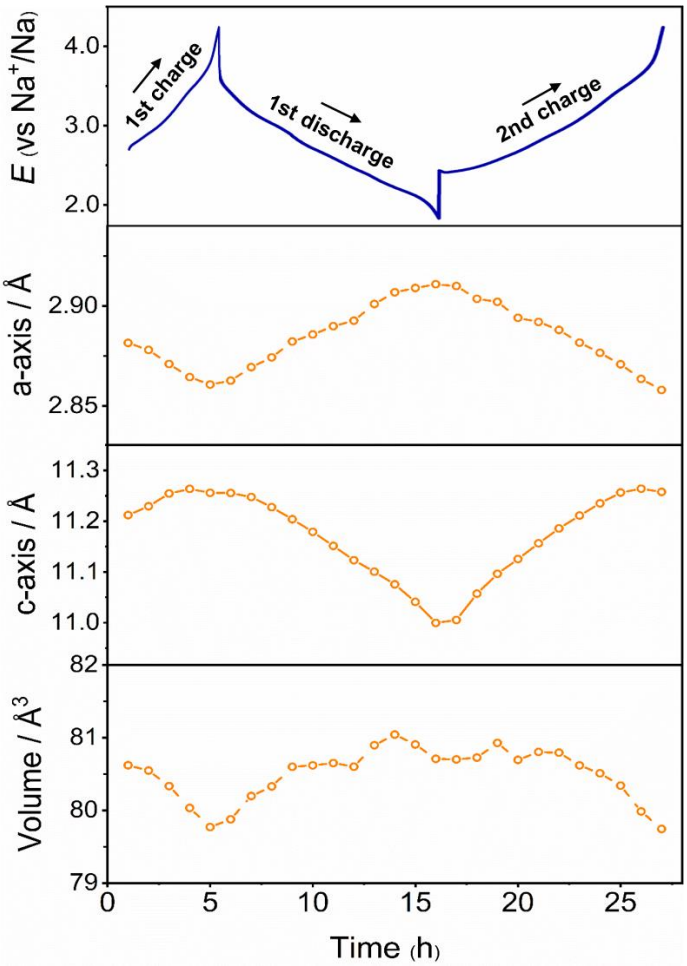

Figure S13. The variation of lattice constants and unit-cell volume along with Na^+ deintercalation and intercalation for NLMT-8.

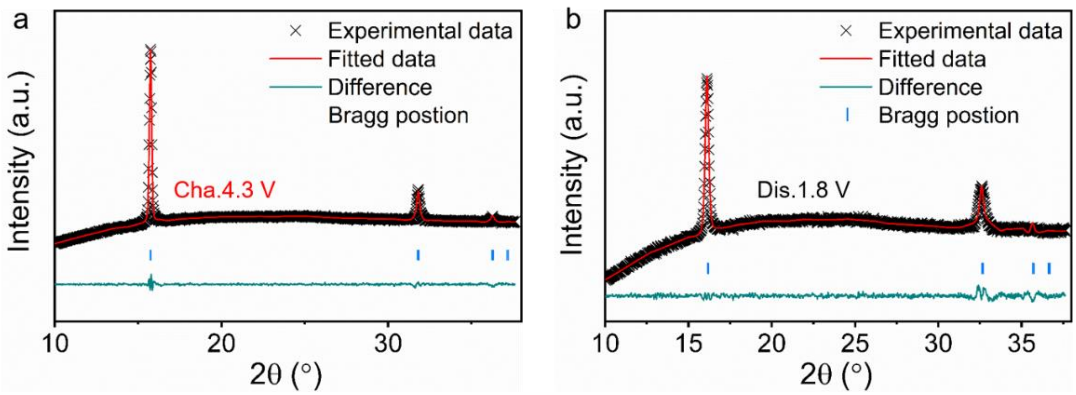

Figure S14. XRD Rietveld refinement patterns for NLMT-8 electrode at the states of (a) 4.3 V-charge and (b) 1.8 V-discharge.

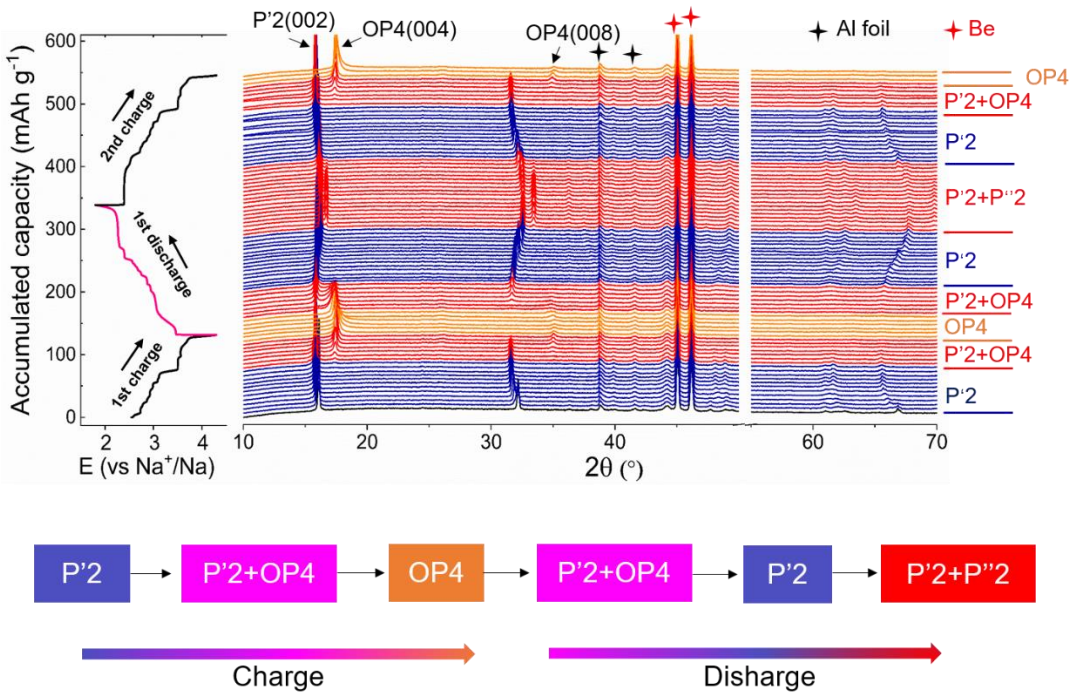

Figure S15. *In-situ* XRD patterns corresponding to the charge and discharge curves of P'2-NM between 1.8 and 4.3 V at 20 mA g^{-1}.

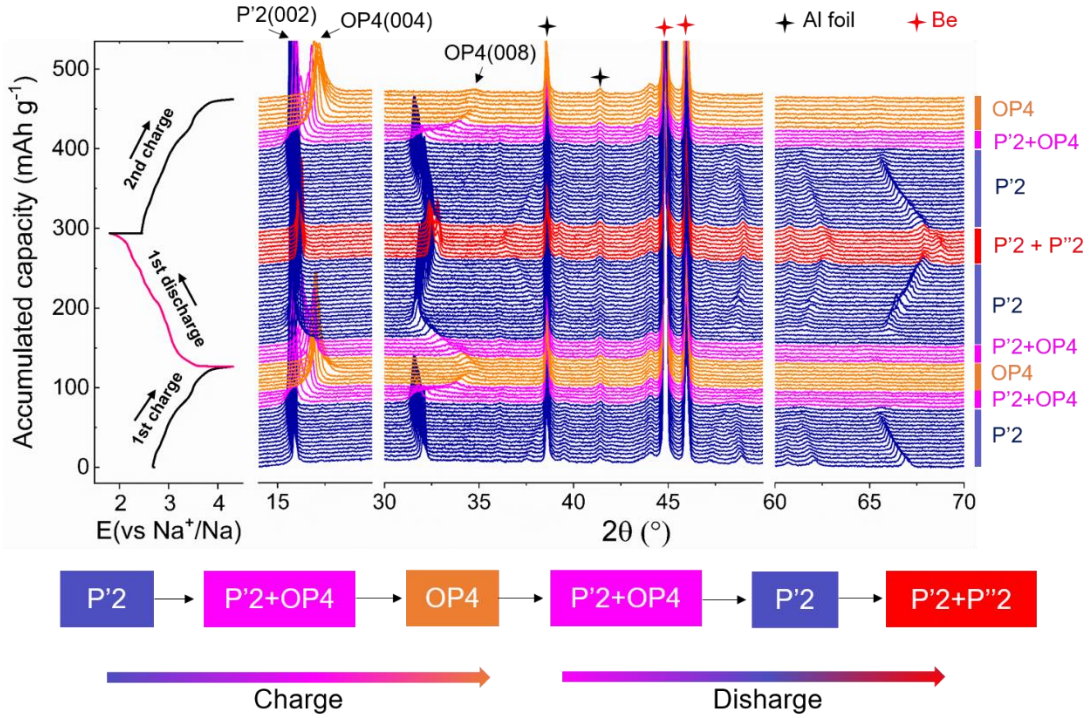

Figure S16. *In-situ* XRD patterns corresponding to the charge and discharge curves of NLMT-0 between 1.8 and 4.3 V at 20 mA g^{-1}.

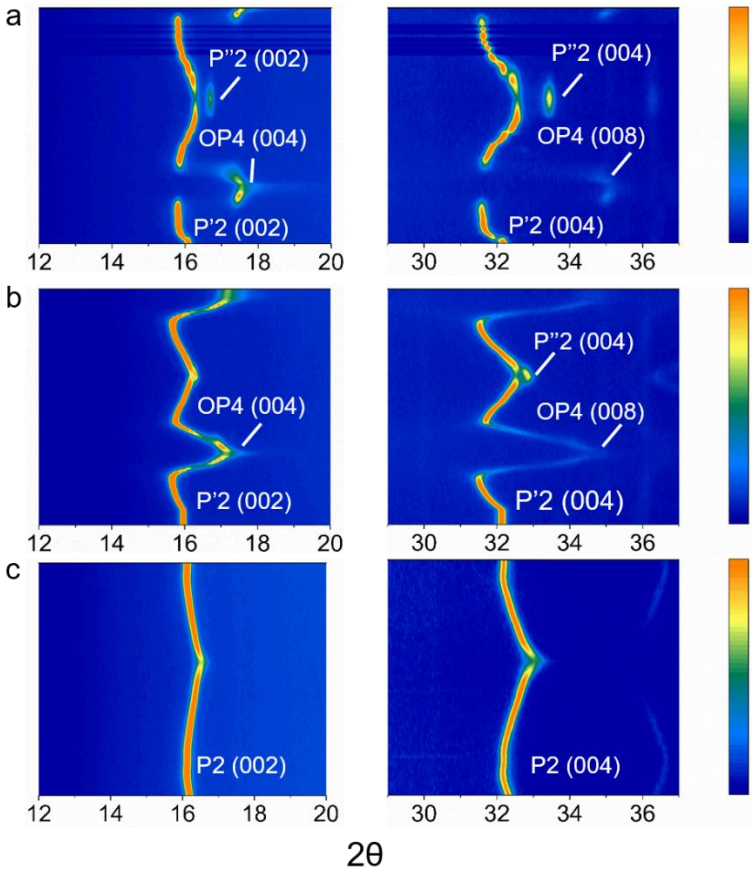

Figure S17. The contour maps of *In-situ* XRD patterns for (a) P'2-NM, (b) NLMT-0 and (c) NLMT-8.

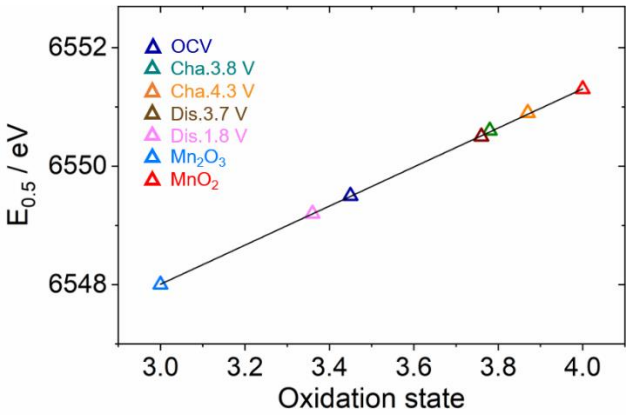

Figure S18. Half-edge energy ($E_{0.5}$) at the Mn K-edges collected at different charge/discharge states.

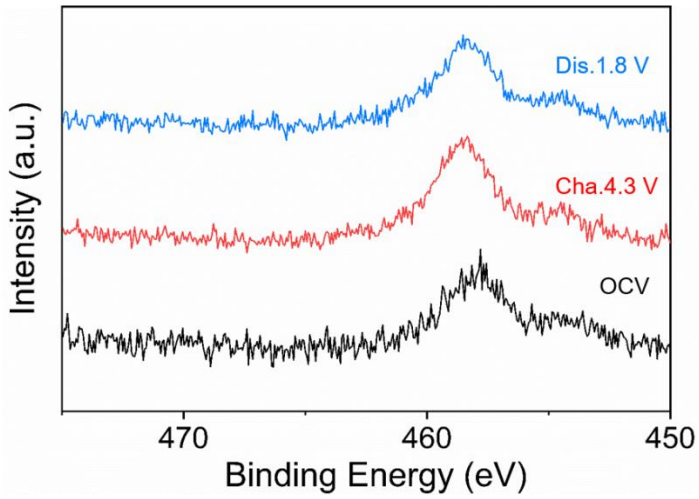

Figure S19. XPS Ti *2p* spectra of NLMT-8 at the states of OCV, 4.3 V-charge and 1.8 V-discharge.

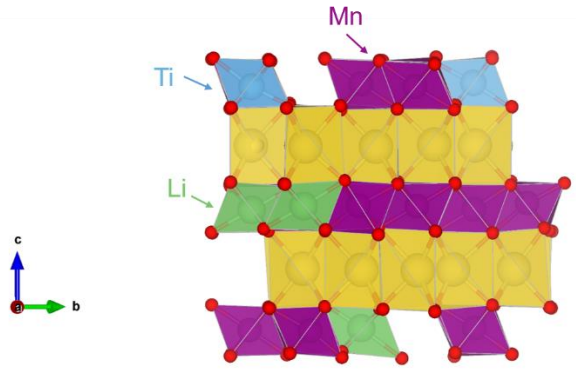

Figure S20. Optimized structure of NLMT-8.

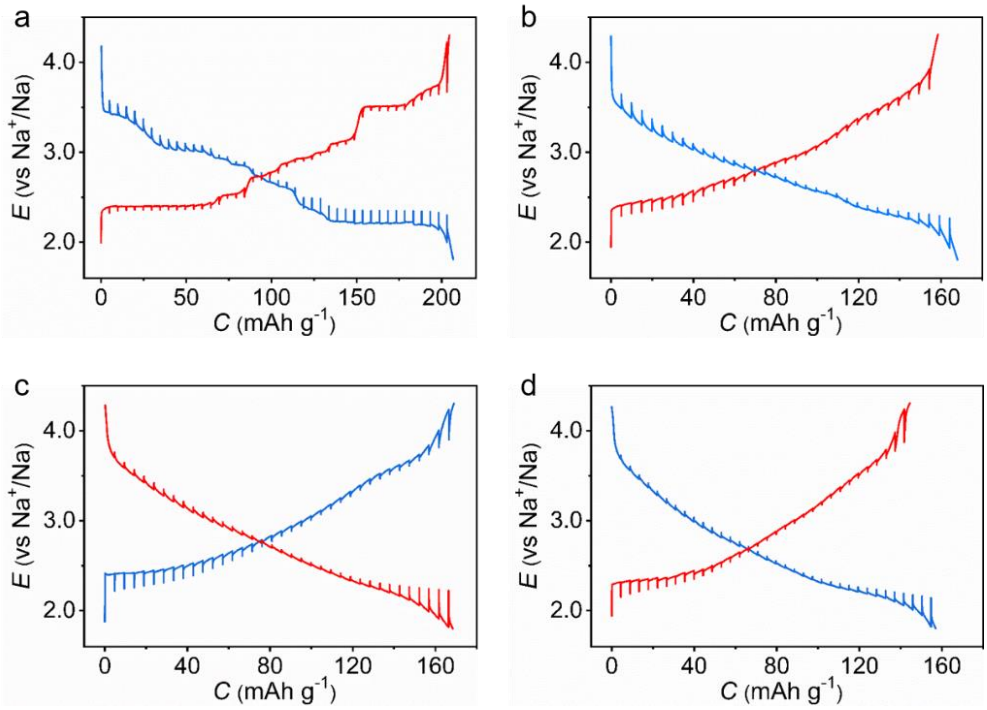

Figure S21. GITT charge/discharge curves of (a) P'2-NM, (b) NLMT-0, (c) NLMT-5 and (d) NLMT-10 between 1.8 and 4.3 V.

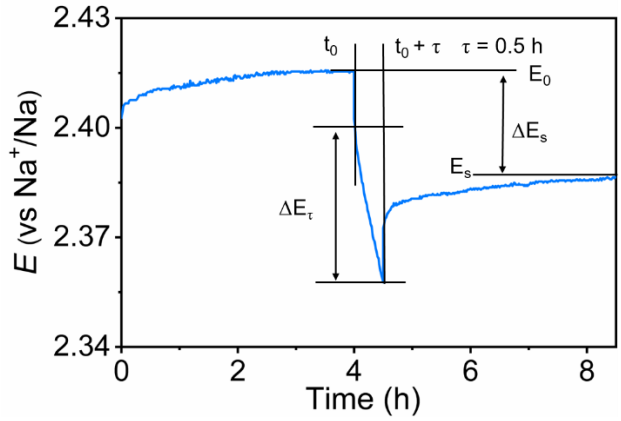

Figure S22. Current step diagrams of NLMT-8 electrode at 2.41 V in the second discharge process. The diffusion coefficient of Na^+ can be determined according to the equation:

$$D_{Na^+} = \frac{4}{\pi\tau}\left(\frac{m_B V_m}{M_B A}\right)^2\left(\frac{\Delta E_s}{\Delta E_\tau}\right)^2$$

Where M_B and m_B represent molecular weight and mass of electrode material, respectively. V_m is the molar volume of active material, and A is area of the electrode. $\triangle E_S$ and $\triangle E\tau$ represent the change in voltage after subtracting the IR drop.

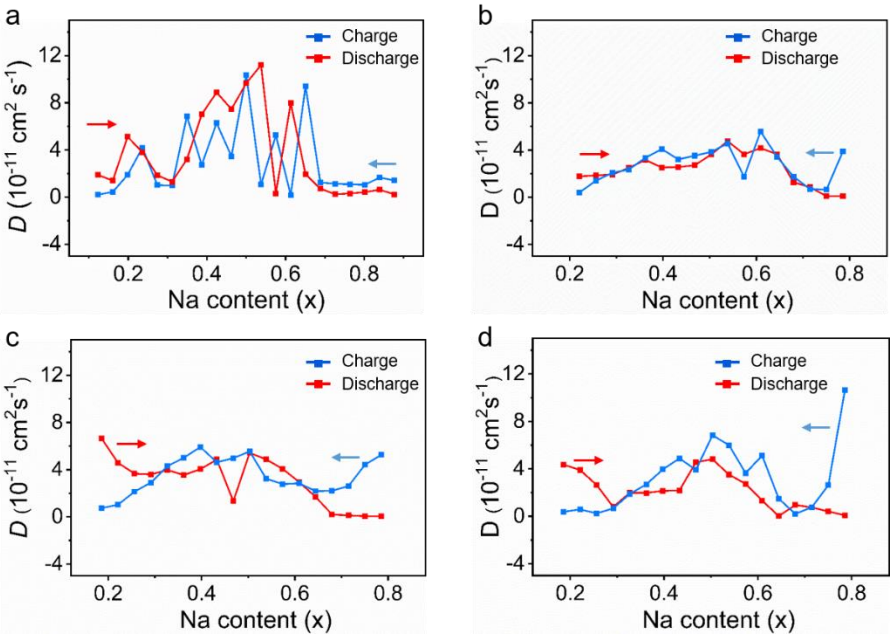

Figure S23. Calculated Na^+ diffusion coefficients of (a) P'2-NM, (b) NLMT-0, (c) NLMT-5 and (d) NLMT-10 electrodes from GITT measurements.

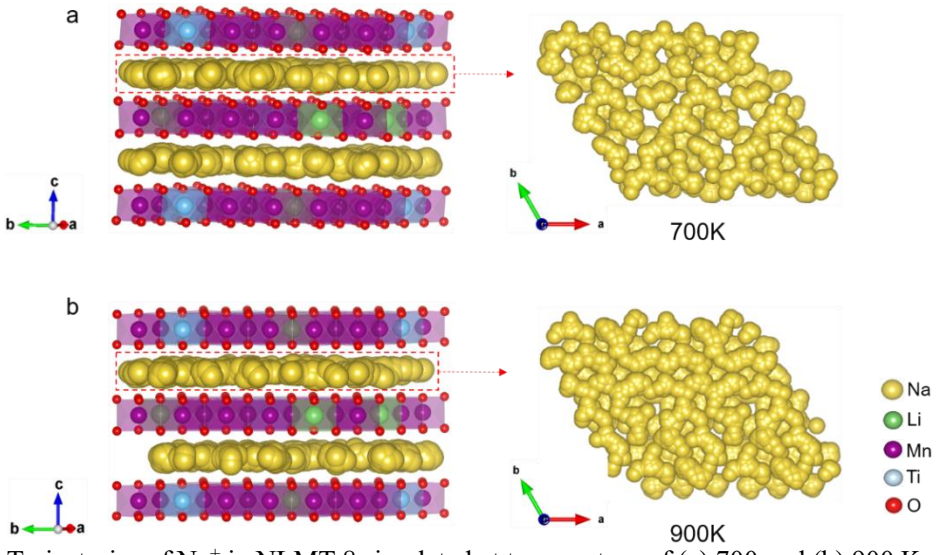

Figure S24. Trajectories of Na^+ in NLMT-8 simulated at temperature of (a) 700 and (b) 900 K.

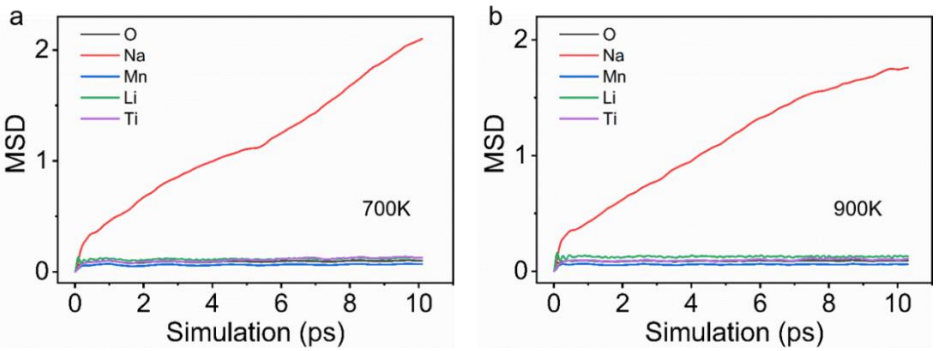

Figure S25. MSDs of Na, Li, Mn, Ti and O as functions of time in NLMT-8 at (a) 700 and (b) 900K.

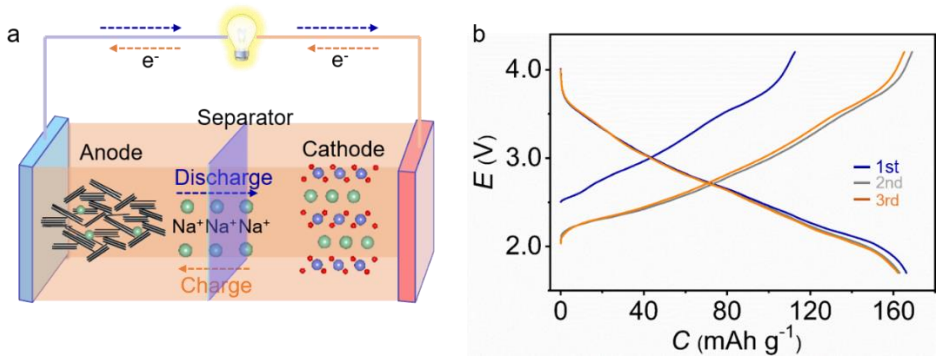

Figure S26. (a) Schematic diagram of the HC//NLMT-8 full cell. (b) Charge/discharge curves for the initial three cycle of the full cell at 25 mA g^{-1}.

Table S1. ICP-OES results of as-prepared samples.

Theoretical chemical formula	Composition from ICP			
	Na	Li	Mn	Ti
$Na_{0.67}MnO_2$	0.649	-	1	-
$Na_{0.67}Mn_{0.90}Ti_{0.10}O_2$	0.630	-	0.908	0.092
$Na_{0.67}Li_{0.05}Mn_{0.85}Ti_{0.10}O_2$	0.653	0.047	0.858	0.095
$Na_{0.67}Li_{0.08}Mn_{0.82}Ti_{0.10}O_2$	0.643	0.078	0.827	0.095
$Na_{0.67}Li_{0.10}Mn_{0.80}Ti_{0.10}O_2$	0.632	0.095	0.806	0.099

Table S2. Structure parameters of P'2-$Na_{0.649}MnO_2$ refined by the Rietveld method.

Sample	Atom	Site	x	y	z	Occ	U_{iso}
P'2-NM	Na_e (1)	4c	0	0.082(4)	0.250	0.256(6)	0.071(5)
	Na_f (2)	4c	0	0.685(3)	0.250	0.383(6)	0.031(0)
	Mn	4a	0	0	0	1	0.019(3)
	O	8f	0	0.666(1)	0.921(3)	1	0.021(6)

Space group: *Cmcm*, a = 2.836 (2) Å, b = 5.248 (4) Å, c = 11.243 (6) Å, α = β = γ= 90°, Vol = 167.342 $Å^3$ (Z = 4), R_P = 2.42%, R_{WP} = 3.32%.

Table S3. Structure parameters of P'2-$Na_{0.630}Mn_{0.908}Ti_{0.092}O_2$ refined by the Rietveld method.

Sample	Atom	Site	x	y	z	Occ	U_{iso}
NLMT-0	$Na_e(1)$	4c	0	0.698(2)	0.250	0.236(4)	0.010(4)
	$Na_f(2)$	4c	0	0.032(2)	0.250	0.452(5)	0.058(3)
	Mn	4a	0	0	0	0.9	0.024(1)
	Ti	4a	0	0	0	0.1	0.010(9)
	O	8f	0	0.659(1)	0.936(1)	1	0.0286(1)

Space group: *Cmcm*, a = 2.849 (2) Å, b = 5.275 (4) Å, c = 11.222 (6) Å, α = β = γ= 90°, Vol = 169.656 $Å^3$, R_P = 1.62%, R_{WP} = 2.32%.

Table S4. Structure parameters of P2/P'2-$Na_{0.653}Li_{0.047}Mn_{0.858}Ti_{0.095}O_2$ refined by the Rietveld method.

Sample	Atom	Site	x	y	z	Occ	U_{iso}
P2 (80.78%)	$Na_e(1)$	2c	0.333	0.666(2)	0.250	0.266(2)	0.055(4)
	$Na_f(2)$	2b	0	0	0.250	0.368(4)	0.071(3)
	Li	2a	0	0	0	0.05	0.003(1)
	Mn	2a	0	0	0	0.85	0.003(1)
	Ti	2a	0	0	0	0.10	0.003(9)
	O	4f	0.333	0.666(1)	0.512(0)	1	0.014(1)
P'2 (19.22%)	$Na_e(1)$	4c	0	0.345(2)	0.250	0.236(4)	0.010(4)
	$Na_f(2)$	4c	0	0.956(2)	0.250	0.502(5)	0.058(3)
	Li	4a	0	0	0	0.05	0.005(1)
	Mn	4a	0	0	0	0.85	0.024(1)
	Ti	4a	0	0	0	0.10	0.010(9)
	O	8f	0	0.660(1)	0.922(0)	1	0.0286(1)

Space group: *Cmcm*, a = 2.848 (2) Å, b = 5.291 (4) Å, c = 11.333 (6) Å, α = β = γ= 90°, Vol = 169.649 $Å^3$, R_P = 1.48%, R_{WP} = 2.30%. *$P6_3/mmc$*, a = 2.734 (4) Å, b = 2.734 (7) Å, c = 11.334 (1) Å, α = β = 90°, γ= 120°, Vol = 72.902 $Å^3$, R_P = 4.26%, R_{WP} = 3.56%.

Table S5. Structure parameters of P2-$Na_{0.643}Li_{0.078}Mn_{0.827}Ti_{0.095}O_2$ refined by the Rietveld method.

Sample	Atom	Site	x	y	z	Occ	U_{iso}
NLMT-8	$Na_e(1)$	2c	0.333	0.666	0.250	0.436(4)	0.08
	$Na_f(2)$	2b	0	0	0.250	0.232(5)	0.12
	Li	2a	0	0	0	0.08	0.01
	Mn	2a	0	0	0	0.82	0.01
	Ti	2a	0	0	0	0.10	0.01
	O	4f	0.333	0.666	0.593(0)	1	0.02

Space group: *$P6_3/mmc$*, a = 2.886 (4) Å, b = 2.886 (7) Å, c = 11.342 (1) Å, α = β = 90°, γ= 120°, Vol = 80.896 $Å^3$, R_P = 6.36%, R_{WP} = 8.86%.

Table S6. Structure parameters of P2-$Na_{0.632}Li_{0.095}Mn_{0.806}Ti_{0.099}O_2$ refined by the Rietveld method.

Sample	Atom	Site	x	y	z	Occ	U_{iso}
NLMT-10	$Na_e(1)$	2c	0.333	0.667(2)	0.250	0.361(4)	0.054(4)
	$Na_f(2)$	2b	0	0	0.250	0.326(5)	0.071(3)
	Li	2a	0	0	0	0.10	0.006(1)
	Mn	2a	0	0	0	0.80	0.006(1)
	Ti	2a	0	0	0	0.10	0.006(9)
	O	4f	0.33333	0.667 (1)	0.585 (0)	1	0.014(1)

Space group: *$P6_3/mmc$*, a = 2.884 (4) Å, b = 2.884 (7) Å, c = 11.306 (1) Å, α = β = 90°, γ= 120°, Vol = 81.508 $Å^3$, R_P = 2.46%, R_{WP} = 1.96%.

Table S7. Atomic distances, slab thickness, Na layer spacing and interslab distance for as-prepared materials.

Parameters	P'2-NM	NLMT-0	NLMT-5		NLMT-8	NLMT-10
Phase	P'2	P'2	P'2[a]	P2[b]	P2	P2
TM-O (Å)	1.900	1.934	1.943	1.924	1.910	1.908
TM-O' (Å)	2.080	1.803	2.039	--	--	--
TMO_2 (Å)	1.972	1.885	1.978	1.895	1.883	1.902
Na layer (Å)	3.649	3.726	3.689	3.772	3.788	3.751
Interslab distance (Å)	5.621	5.611	5.667	5.667	5.671	5.653

a: 19.22 wt%; b:80.78 wt%

Table S8. Curvefit parameters at the Mn K-edge EXAFS for NLMT-0 samples.

Path	d^b /Å	*N*	*R*/Å	σ^2/Å^2
Mn-O1	1.882	4	1.870	0.002
Mn-O2	1.957	2	1.971	0.002
Mn-Mn1	2.833	4	2.799	0.002
Mn-Mn2	2.982	2	2.953	0.002

S_0^2 for this fit is 0.5. ΔE_0 was refined as a global fit parameter. Data ranges: $2.5 \leq k \leq 10$ Å^{-1}, $1.0 \leq R \leq 3.0$ Å. The number of variable parameters is 7. R factor for this fit is 1.79 %. [b] The distances for Mn-O and Mn-Mn are from the crystal structure of P'2-$Na_{0.67}MnO_2$. The Debye Waller factors were constrained as σ^2(Mn-O1) = σ^2(Mn-O2) = σ^2(Mn-Mn1) = σ^2(Mn-Mn2) for reducing the number of variables.

Table S9. Curvefit parameters at the Mn K-edge EXAFS for NLMT-8 samples.

Path	*d* /Å	*N*	*R*/Å	σ^2/Å^2
Mn-O	1.835	6	1.902	0.007
Mn-Mn	2.845	6	2.906	0.010

S_0^2 for this fit is 0.7. ΔE_0 was refined as a global fit parameter. Data ranges: $2.5 \leq k \leq 10$ Å^{-1}, $1.0 \leq R \leq 3.0$ Å. The number of variable parameters is 7. R factor for this fit is 0.89 %. [b] The distances for Mn-O and Mn-Mn are from the crystal structure of P2-$Na_{0.67}MnO_2$. The Debye Waller factors were constrained as σ^2(Mn-O) = σ^2(Mn-Mn) for reducing the number of variables.

Table S10. Structure parameters of P2-$Na_{0.221}Li_{0.078}Mn_{0.827}Ti_{0.095}O_2$ refined by the Rietveld method.

Sample	Atom	Site	x	y	z	Occ	U_{iso}
NLMT-8	$Na_e(1)$	2c	0.333	0.666	0.250	0.115	0.05
	$Na_f(2)$	2b	0	0	0.250	0.105	0.07
	Li	2a	0	0	0	0.08	0.01
	Mn	2a	0	0	0	0.82	0.01
	Ti	2a	0	0	0	0.10	0.01
	O	4f	0.333	0.666	0.486(2)	1	0.02

Space group: *P6₃/mmc*, a = 2.859 (3) Å, b = 2.859 (2) Å, c = 11.252 (2) Å, α = β = 90°, γ= 120°, Vol = 79.690 $Å^3$, R_P = 4.26%, R_{WP} = 5.36%.

Table S11. Structure parameters of P2-$Na_{0.821}Li_{0.078}Mn_{0.827}Ti_{0.095}O_2$ refined by the Rietveld method.

Sample	Atom	Site	x	y	z	Occ	U_{iso}
NLMT-8	$Na_e(1)$	2c	0.333	0.666	0.250	0.427	0.05
	$Na_f(2)$	2b	0	0	0.250	0.393	0.07
	Li	2a	0	0	0	0.08	0.01
	Mn	2a	0	0	0	0.82	0.01
	Ti	2a	0	0	0	0.10	0.01
	O	4f	0.333	0.666	0.509(3)	1	0.02

Space group: *P6₃/mmc*, a = 2.907 (3) Å, b = 2.907 (2) Å, c = 10.982 (2) Å, α = β = 90°, γ= 120°, Vol = 80.374 $Å^3$, R_P = 3.16%, R_{WP} = 2.38%.

Table S12. Curvefit parameters at the Mn K-edge EXAFS for NLMT-8 at different charge and discharge states.

Samples	Path	*d* /Å	*N*	*R*/Å	σ^2/Å^2
OCV	Mn-O	1.835	6	1.906	0.003
	Mn-TM	2.845	6	2.913	0.005
Cha.3.8V	Mn-O	1.835	6	1.902	0.002
	Mn-TM	2.845	6	2.898	0.003
Cha.4.3V	Mn-O	1.835	6	1.899	0.002
	Mn-TM	2.845	6	2.882	0.004
Dis.3.7V	Mn-O	1.835	6	1.900	0.002
	Mn-TM	2.845	6	2.884	0.004
Dis.1.8V	Mn-O	1.835	6	1.896	0.002
	Mn-TM	2.845	6	2.892	0.005

Table S13. ICP-OES results for cycled NLMT-8 samples.

Theoretical chemical formula	Composition from ICP			
	Na	Li	Mn	Ti
1st-cha. 4.3V	0.221	0.070	0.843	0.087
1st-dis. 1.8V	0.821	0.068	0.845	0.087
After 50 cycles	0.789	0.067	0.847	0.086